

Molecular and Neural Functions of *Rai1*, the Causal Gene for Smith-Magenis Syndrome

Highlights

- *Rai1* preferentially binds active promoters and promotes transcription
- Pan-neural loss of *Rai1* causes motor function and learning deficits and obesity
- *Rai1* loss in inhibitory and subcortical excitatory neurons causes learning deficits
- *Rai1* loss in subcortical excitatory, Sim1⁺, and SF1⁺ neurons causes obesity

Authors

Wei-Hsiang Huang,
Casey J. Guenther, Jin Xu, ...,
Howard Y. Chang, Mehrdad Shamloo,
Liquan Luo

Correspondence

weihsiah@stanford.edu (W.-H.H.),
lluo@stanford.edu (L.L.)

In Brief

Huang et al. show that *Rai1*, the causal gene for neurodevelopmental disorder Smith-Magenis syndrome (SMS), binds active promoters and promotes transcription. *Rai1* loss in different neuronal subtypes gives rise to specific SMS-like deficits in motor function, learning, and food intake.

Molecular and Neural Functions of *Rai1*, the Causal Gene for Smith-Magenis Syndrome

Wei-Hsiang Huang,^{1,2,7,*} Casey J. Guenther,^{1,2,3,7} Jin Xu,^{4,7} Tiffany Nguyen,⁵ Lindsay A. Schwarz,^{1,2} Alex W. Wilkinson,² Or Gozani,² Howard Y. Chang,⁴ Mehrdad Shamloo,^{5,6} and Liqun Luo^{1,2,3,8,*}

¹Howard Hughes Medical Institute

²Department of Biology

³Neurosciences Program

⁴Center for Personal Dynamic Regulomes and Program in Epithelial Biology

⁵Stanford Behavioral and Functional Neuroscience Laboratory

⁶Department of Neurosurgery

Stanford University, Stanford, CA 94305, USA

⁷Co-first author

⁸Lead Contact

*Correspondence: weihsiah@stanford.edu (W.-H.H.), lluo@stanford.edu (L.L.)

<http://dx.doi.org/10.1016/j.neuron.2016.09.019>

SUMMARY

Haploinsufficiency of *Retinoic Acid Induced 1 (RAI1)* causes Smith-Magenis syndrome (SMS), which is associated with diverse neurodevelopmental and behavioral symptoms as well as obesity. *RAI1* encodes a nuclear protein but little is known about its molecular function or the cell types responsible for SMS symptoms. Using genetically engineered mice, we found that *Rai1* preferentially occupies DNA regions near active promoters and promotes the expression of a group of genes involved in circuit assembly and neuronal communication. Behavioral analyses demonstrated that pan-neural loss of *Rai1* causes deficits in motor function, learning, and food intake. These SMS-like phenotypes are produced by loss of *Rai1* function in distinct neuronal types: *Rai1* loss in inhibitory neurons or subcortical glutamatergic neurons causes learning deficits, while *Rai1* loss in *Sim1*⁺ or *SF1*⁺ cells causes obesity. By integrating molecular and organismal analyses, our study suggests potential therapeutic avenues for a complex neurodevelopmental disorder.

INTRODUCTION

Copy number variations (CNVs) cause numerous neurodevelopmental and psychiatric disorders (Malhotra and Sebat, 2012; Ramocki and Zoghbi, 2008). It is generally difficult to dissect the etiology and develop effective treatments for disorders associated with large CNVs due to uncertainty about which genes within a deletion or duplication are responsible for the symptoms (Zhang et al., 2009). A prominent CNV disorder is Smith-Magenis syndrome (SMS) (Smith et al., 1986), which affects one in ~15,000 individuals. SMS patients exhibit craniofacial abnormalities, obesity, circadian abnormality, hypotonia, intellectual

disabilities, stereotypies, and autistic features (Greenberg et al., 1996; Smith et al., 1993). 70% of SMS patients have an ~3.7 Mb interstitial deletion of chromosome 17p11.2 that contains 76 genes (Elsea and Girirajan, 2008). Importantly, 10% of SMS patients harbor point mutations or small deletions causing haploinsufficiency of a single gene within this region, *Retinoic Acid Induced 1 (RAI1)* (Dubourg et al., 2014; Slager et al., 2003). Patients with *RAI1* mutations exhibit almost all of the core features of SMS, indicating that *RAI1* is the dosage-sensitive gene responsible for most symptoms even in patients with large deletions. Furthermore, the reciprocal duplication in 17p11.2 causes Potocki-Lupski syndrome (PTLS), which shares many neuropsychological symptoms with SMS (Potocki et al., 2000, 2007). The smallest region common to PTLS patients with different duplications is a 125-kb region containing only *RAI1* (Zhang et al., 2010), suggesting that duplication of *RAI1* may also be responsible for the symptoms of PTLS. Therefore, brain development and function is exquisitely sensitive to *RAI1* copy number.

RAI1 is a nuclear protein with two predicted protein-interacting domains: an extended plant homeo-domain (ePHD) and a nucleosome-binding domain (NBD) (Darvekar et al., 2012, 2013). In vitro studies revealed that overexpressed *RAI1* associates with nuclear structures with high affinity (Darvekar et al., 2012). Furthermore, the *RAI1* NBD can interact with HeLa nucleosomes (Darvekar et al., 2013). Overexpressed *RAI1* binds to *Brain-Derived Growth Factor (BDNF)* and *Circadian Locomotor Output Cycles Kaput (CLOCK)* enhancers in vitro (Burns et al., 2010; Williams et al., 2012). While *RAI1* does not possess a known DNA binding domain, when fused with a GAL4 DNA-binding domain, *RAI1* shows moderate transcriptional activity in a luciferase assay (Bi et al., 2005). Although these data suggest a role for *RAI1* in transcriptional regulation, its in vivo mode of action and targets remain unknown.

Mouse models have been used to study *Rai1* function in vivo. Using an *Rai1*^{LacZ/+} allele that expresses β -galactosidase from the mouse *Rai1* locus, it was found that *Rai1* is expressed in many tissues including the developing and adult nervous system (Bi et al., 2005). Most *Rai1* null mice die in utero; the few that survive exhibit craniofacial and skeletal abnormalities, motor

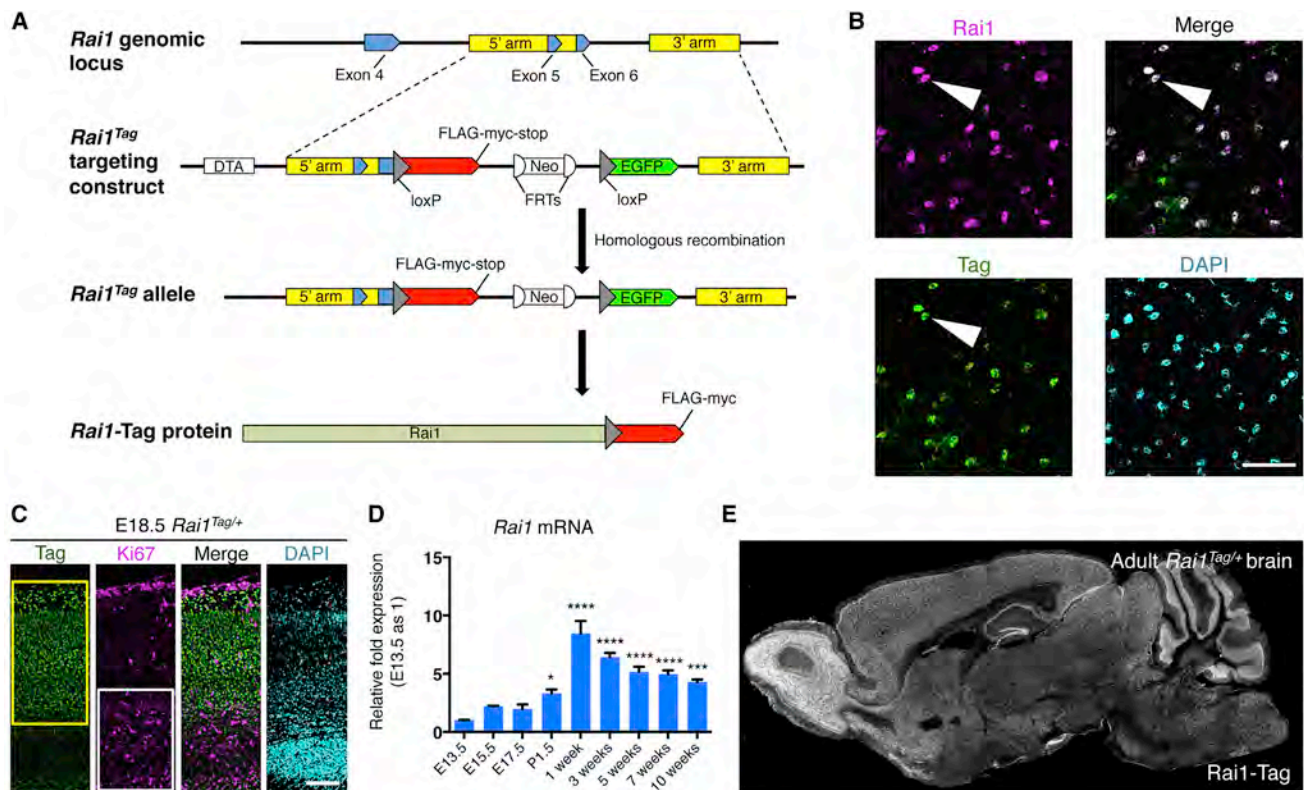


Figure 1. Spatial and Temporal Expression Patterns of Rai1

(A) Strategy to generate the Rai1-Tag mice. In the wild-type *Rai1* genomic locus (first row), yellow boxes indicate the 5' and 3' arms for homologous recombination. Blue boxes indicate the *Rai1* exons. Embryonic stem cells were injected with the *Rai1*^{Tag} targeting construct (second row) to generate the *Rai1*^{Tag} allele (third row) encoding an Rai1-FLAG-myc fusion protein (Rai1-Tag; the Tag follows the last amino acid of Rai1 before the natural stop codon). Neomycin (Neo) and diphtheria toxin A (DTA) cassettes were used for positive and negative selection, respectively.

(B) P21 *Rai1*^{Tag/+} cortex showing that Rai1 (magenta, detected by an anti-Rai1 antibody) and Rai1-Tag (green, detected by an anti-FLAG antibody) are co-localized in the nucleus (merged in white). White arrowheads indicate an Rai1⁺/Tag⁺/DAPI⁺ cell. DAPI staining (cyan) represents all nuclei. Scale bar, 50 μm.

(C) E18.5 *Rai1*^{Tag/+} cortex showing that Rai1-Tag (green) is expressed in the cortical plate enriched for postmitotic neurons (yellow box) but rarely in the Ki67⁺ (magenta) dividing cells (white box). DAPI staining (cyan) represents all nuclei. Scale bar, 100 μm.

(D) qRT-PCR showing that during mouse cortical development, *Rai1* mRNA levels increase as neurons mature. Data are mean ± SEM. *p < 0.05, ***p < 0.001, ****p < 0.0001 (n = 3) when compared to E13.5 using Bonferroni post hoc test following a significant ANOVA.

(E) Sagittal section of adult *Rai1*^{Tag/+} mouse brain showing that Rai1-Tag protein (white) is widely expressed in olfactory bulb, cortex, hippocampus, striatum, thalamus, hypothalamus, cerebellum, and brainstem. Most blank regions are axon fibers (white matter). See also Figure S1.

dysfunction, and fear-learning deficits (Bi et al., 2007). *Rai1* heterozygous mice display mild SMS-like symptoms including obesity, circadian abnormalities, and characteristic craniofacial features (Bi et al., 2005; Lacaria et al., 2013). Overexpression of Rai1 in mice results in growth retardation, hyperactivity, and motor deficits (Girirajan et al., 2008). Given the broad expression pattern of Rai1 and diverse SMS symptoms, it is critical to determine whether specific symptoms are results of Rai1 requirement in specific cell types, in order to understand SMS pathogenesis and develop targeted therapies. Furthermore, while removing one copy of *Rai1* better mimics the genetic underpinnings of SMS, deleting both copies in specific cell types may result in more severe phenotypes that reveal biological functions of Rai1.

Here, we have taken an integrative approach to dissect the molecular and neural functions of Rai1. Using a *Rai1* conditional allele and an epitope-tagged *Rai1* allele, we found that Rai1

preferentially occupies DNA regions near active promoters and enhances the expression of genes that function in cell-cell communication. We identified cell types that require Rai1 for proper motor function, learning, and food intake. Our integrative approach provides mechanistic insights into the etiology of SMS and suggests specific therapeutic strategies.

RESULTS

Rai1 Is Broadly Expressed in Postmitotic Neurons

To characterize Rai1 expression and to analyze its molecular functions, we engineered knockin mice with tandem FLAG and myc peptides (hereafter, Tag) fused to the carboxyl terminus of endogenous Rai1 (Rai1-Tag; Figure 1A). Western blot showed that the anti-FLAG antibody specifically recognized Rai1-Tag but not endogenous Rai1 (Figure S1A). Rai1-Tag was expressed

at a similar level as un-tagged Rai1 (Figure S1B), as shown by an anti-Rai1 antibody we developed (and validated by lack of staining in conditional knockout; see below). Immunostaining revealed that Rai1-Tag co-localized with signals detected by the anti-Rai1 antibody in the postnatal day (P) 21 somatosensory cortex (white arrowheads, Figure 1B). 99.6% Rai1⁺ cells expressed Tag, 98.2% of the Tag⁺ cells expressed Rai1 (Figure 1B; quantified from 1,432 DAPI⁺ cells from 9 sections). We conclude that Rai1-Tag faithfully represents the endogenous Rai1 expression and used Rai1-Tag to further characterize Rai1 expression.

Consistent with a previous report (Bi et al., 2005), we observed Rai1-Tag expression in the embryonic day 9.5 (E9.5) branchial arch (Figure S1C) that develops into craniofacial structures. In E18.5 cortex, Rai1-Tag was broadly expressed in the cortical plate enriched in postmitotic neurons but rarely in the Ki67⁺ actively dividing cells near the ventricular zone (Figure 1C). The enrichment of Rai1 in postmitotic but not in proliferating cells was also observed in the developing dentate gyrus (Figure S1D and Table S1), cerebellum, and olfactory cortex (data not shown). Rai1 was also detected in a small fraction of S100β⁺ cerebellar Bergmann glia (Figure S1E and Table S1). Consistent with immunostaining, qRT-PCR using mouse cortices indicated that *Rai1* mRNA levels increased during prenatal development, peaked around 1 week after birth, and persisted into adulthood (Figure 1D). Rai1-Tag was broadly expressed throughout the adult mouse brain (Figure 1E) and co-localized with 78% of the NeuN⁺ cortical neurons (Figure S1F and Table S1). Rai1 is expressed in both excitatory and inhibitory neurons in the thalamus (Figures S1G–S1J) and cortex (Figures S1K and S1L). Quantification based on double labeling of Rai1-Tag and in situ hybridization showed that Rai1 is expressed in 75% of excitatory neurons expressing *Vglut1* (encoding vesicular glutamate transporter 1) and 57% of inhibitory neurons expressing *Gad1* and/or *Gad2* (encoding glutamate decarboxylases) in cortex (Figures S1K and S1L and Table S1). In summary, Rai1 is expressed in many cell types in the brain, with an onset that parallels the neuronal differentiation process.

Rai1 Occupies DNA Regions Near Active Promoters In Vivo

Mouse Rai1 and human RAI1 share the same protein structure, with 82% overall sequence identity, and 88% and 82% identity in the C-terminal NBD and ePHD, respectively (Figure 2A). Human RAI1^{NBD} was shown to interact with nucleosomes in vitro (Darvekar et al., 2013). To further characterize molecular functions of Rai1, we purified the recombinant human and mouse NBDs and ePHDs expressed in *E. coli* and performed a nucleosome pull-down assay. We found that NBDs from both species interact with HeLa nucleosomes, whereas an equal amount of ePHD protein did not (Figures 2B, S2A, and S2B). In a cellular fractionation assay using mouse cortices, Rai1 was present in both nucleoplasmic and chromatin-binding fractions (Figure 2C). These experiments suggest that Rai1 interacts with chromatin in vitro and in vivo.

To investigate the genome-wide DNA binding pattern of Rai1 in vivo, we performed chromatin immunoprecipitation coupled with high-throughput sequencing (ChIP-seq) using *Rai1*^{Tag/+} mice. After confirming that FLAG-tagged Rai1 was enriched in

anti-FLAG immunoprecipitation (Figure S2C), we performed ChIP-seq using 8-week-old *Rai1*^{Tag/+} mouse cortices. We obtained ~35 million paired-end reads, which exhibited a bimodal enrichment pattern along the mouse genome for each of the two replicas (Figure S2D and Table S2). We identified ~15,000 reproducible peaks (Irreproducible Discovery Rate < 0.05) as high-confidence Rai1 binding sites (Figure S2E and Table S3). ChIP-qPCR also validated Rai1 binding sites identified by ChIP-seq (Figure S2F). Genome-wide enrichment analysis revealed that Rai1 binding sites were enriched in CpG islands, 5' UTRs, and promoters (Figure 2D), but not intergenic or repetitive regions (Figure S2G). Normalized Rai1 ChIP-seq read densities on RefSeq gene bodies showed strong enrichment around transcriptional start sites (TSSs) (Figure 2E). These results demonstrate that Rai1 preferentially occupies promoter regions. We then categorized regions of the mouse genome into different states based on combinations of active or repressive chromatin marks (Ernst and Kellis, 2012). The overlay of Rai1 binding sites with different chromatin states further indicated that Rai1 binds active promoter and enhancer regions (Figures 2F and S2H; Table S4).

To determine the specificity of Rai1 binding to different DNA sequences, we applied a de novo motif-discovery algorithm (Heinz et al., 2010) on the high-confidence Rai1 binding sites. Among the significantly over-represented motifs (Figure S2I), an 8-mer motif was found in 45% Rai1 binding sites (Figure 2G; $p = 1e-58$). A comparison with previously discovered DNA motifs revealed that the 8-mer motif resembles the consensus sequences bound by zinc finger transcription factors ZNF711 and Zfx (Figure 2G). Interestingly, *ZNF711* is highly expressed in the brain (Kleine-Kohlbrecher et al., 2010), and truncating mutations of *ZNF711* have been identified in X-linked mental retardation (Tarpey et al., 2009). It remains to be experimentally determined whether these similar binding motifs are a consequence of physical interactions between Rai1 and ZNF711/Zfx, or could result in their competition. Comparisons of the positions between Rai1 peaks with existing mouse Zfx ChIP-seq data (Chen et al., 2008) revealed that Zfx binding signals and Rai1 peaks were globally co-localized, along with RNA polymerase 2 (Pol2) binding sites and the permissive transcription mark H3K4me3 (Figure 2H). By ranking the ChIP-seq peaks based on Rai1 peak intensity, we generated a heatmap showing the corresponding ChIP-seq read intensities of H3K4me3, Pol2, Zfx, and a negative control (anti-GFP antibody) (Figure 2I). The heatmap showed a high co-occupancy between Rai1 peaks with H3K4me3, Pol2, and Zfx peaks, but not with the negative control. Together, our genome-wide analysis indicates that Rai1 binds to specific loci in the genome associated with active transcription.

Rai1 Positively Regulates Steady-State Transcription

Given that Rai1 binds to promoter regions, we next examined how loss of Rai1 impacts the transcriptome. To circumvent embryonic lethality of *Rai1* null mice, we generated a conditional knockout (CKO) allele by flanking exon 3, which encodes 97% of the *Rai1* open reading frame including the translational start, with *loxP* sites (Figures S3A and S3B). *Rai1*^{lox/lox} mice were born at the expected Mendelian ratio without apparent abnormalities. We then conditionally deleted *Rai1* in the nervous

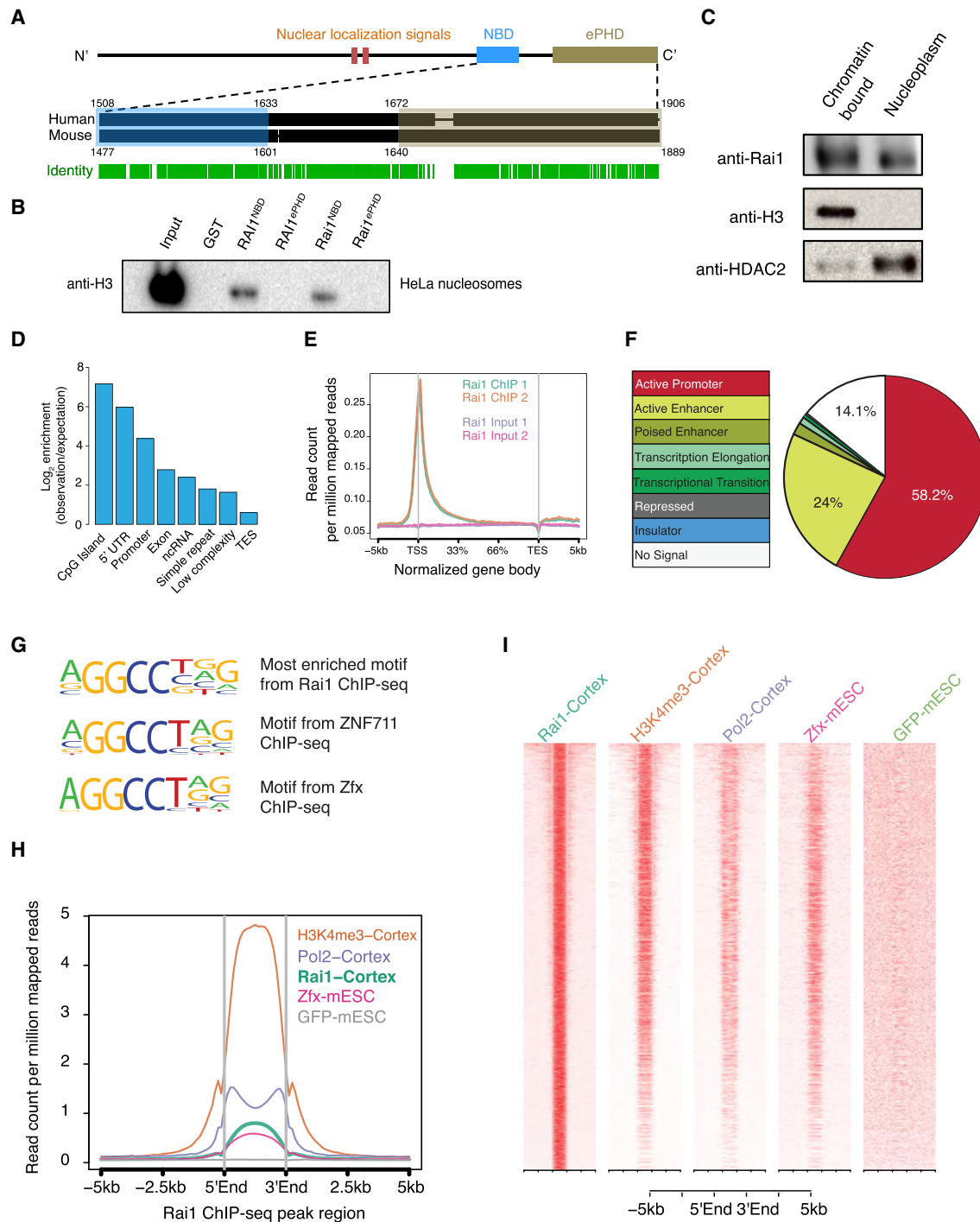


Figure 2. Rai1 Preferentially Occupies the Promoter Regions of Active Chromatin

(A) Schematic representation of predicted Rai1 protein domains. The nucleosome binding domain (NBD, blue) and extended plant homeo-domain (ePHD, brown) of human RAI1 and mouse Rai1 show a high degree of sequence conservation (identical amino acids are indicated as vertical green lines at bottom). In the magnified C termini of both proteins, numbers indicate amino acids in the primary sequence, and thin lines indicate gaps in alignment.

(B) In vitro nucleosome interaction assay showing that both human and mouse NBDs, but not ePHDs, bind purified HeLa nucleosomes.

(C) Cellular fractionation assay using mouse cortex showing that endogenous Rai1 co-fractionated with both histone H3 (chromatin fraction) and HDAC2 (nucleoplasmic fraction).

(D) Genome-wide annotation showing Rai1 binding sites identified by CHIP-seq are highly enriched at CpG island, 5' UTR, and promoter regions. ncrRNA, non-coding RNA; TES, transcription end site.

(legend continued on next page)

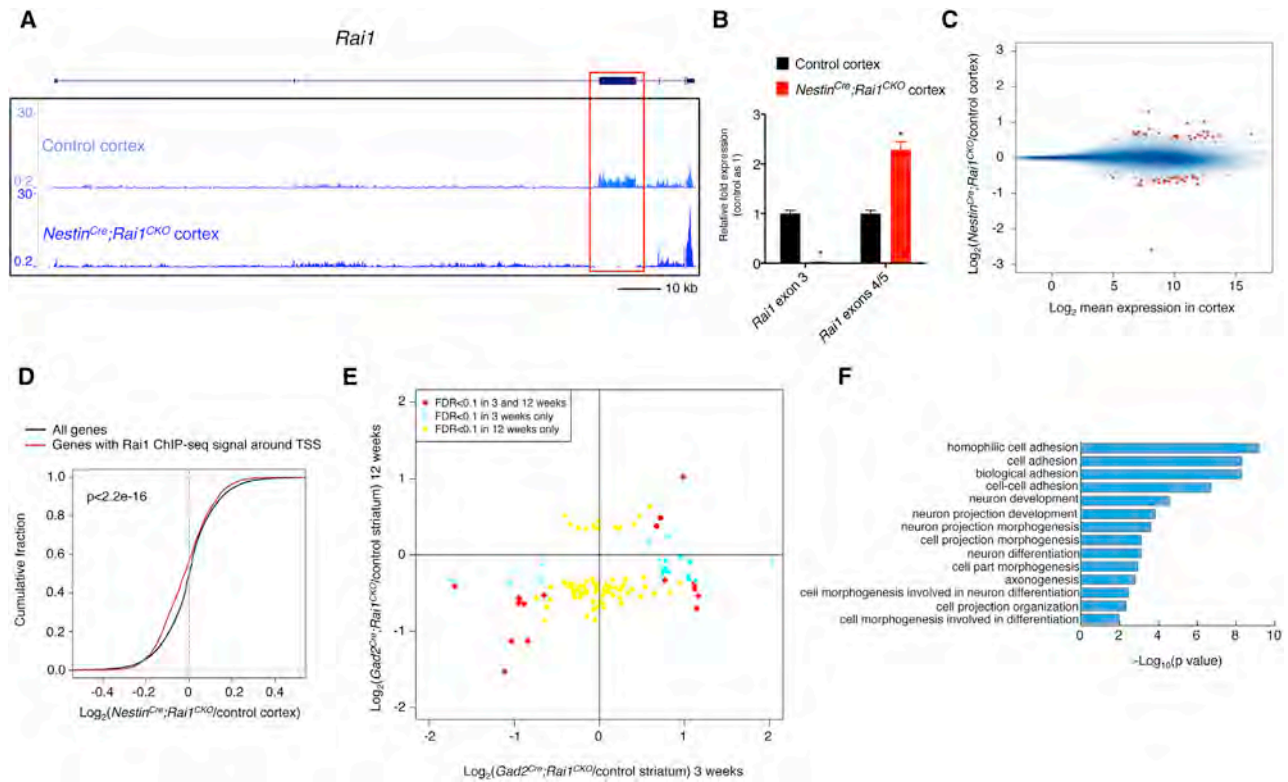


Figure 3. Transcriptomic Changes in *Rai1* Mutant Brains

(A) UCSC browser tracks of the cortex RNA-seq data of the *Rai1* locus. The expression of floxed exon 3 (red box) is largely absent in the *Nestin^{Cre};Rai1^{CKO}* cortex, while exons 4 to 6 are all upregulated compared to control. Coding exons, tall boxes.

(B) qRT-PCR showing Cre-dependent decrease of *Rai1* exon 3 mRNA expression, and upregulation of *Rai1* exons 4/5. Data are mean \pm SEM (* $p < 0.05$, unpaired t test, $n = 3$).

(C) Genome-wide gene expression change in 3-week-old *Nestin^{Cre};Rai1^{CKO}* cortex compared to control. Red dots show genes with False Discovery Rate (FDR) < 0.05 and brown dots show genes with $0.05 < \text{FDR} < 0.1$.

(D) Genes with *Rai1* binding sites identified by ChIP-seq in cortex showing a leftward shift in the cumulative distribution plot (red) compared with cumulative distribution of all genes (black), suggesting a global downregulation of *Rai1*-bound genes in the *Rai1* mutant cortex.

(E) Downregulated genes in *Gad2^{Cre};Rai1^{CKO}* striatum at 3 weeks are still downregulated at 12 weeks (red dots in the bottom left but not top left quadrants). However, several 3-week upregulated genes become significantly downregulated at 12-weeks (red dots in the bottom right quadrant).

(F) Gene ontology analysis of downregulated genes in cortex and striatum showing enrichment in cell adhesion and morphogenesis-related terms. Gene ontology terms are ranked by FDR.

See also [Figure S3](#).

system using a pan-neural *Nestin^{Cre}* line (Tronche et al., 1999). Western blot analysis using an anti-*Rai1* antibody confirmed that *Rai1* protein was undetectable in *Nestin^{Cre};Rai1^{CKO}* brains (Figure S3C).

As *Nestin^{Cre};Rai1^{CKO}* mice exhibited postnatal lethality at increasing frequency with age (see below), we performed

RNA sequencing (RNA-seq) using cortices from 3-week-old *Rai1^{fllox/fllox}* (control) and *Nestin^{Cre};Rai1^{CKO}* mice. RNA-seq (Figure 3A) and qRT-PCR (Figure 3B) confirmed that exon 3 of *Rai1* was deleted in the *Nestin^{Cre};Rai1^{CKO}* cortices. Unexpectedly, the expression of small exons 3' to the deleted region of *Rai1* was upregulated (Figures 3A and 3B), possibly due to

(E) Normalized *Rai1* ChIP-seq signals compared to inputs on UCSC mm9 RefSeq gene bodies showing higher signal around the transcription start sites (TSSs). Gene bodies were normalized to 0%–100% as relative positions.

(F) Annotation of *Rai1* binding sites identified by ChIP-seq, using multiple chromatin marks. Functional regions are defined using ENCODE ChIP-seq data from 8-week-old cortex by ChromHMM (see [Supplemental Experimental Procedures](#)).

(G) The most enriched motif among *Rai1* binding sites (45% of total) predicted by de novo motif analysis (top) using high-confidence *Rai1* peaks. The *Rai1* motif is highly similar to that of zinc-finger transcription factors ZNF711 (middle) and Zfx (bottom).

(H) *Rai1* ChIP-seq peak regions (from 5' to 3' end) showing an enrichment of binding sites for H3K4me3, RNA polymerase 2 (Pol2) (cortex data from mouse ENCODE), and Zfx (mouse embryonic stem cell [mESC]; Chen et al., 2008), but not GFP (negative control). Peak regions in the middle were normalized to 0%–100% as relative position from 5' to 3' end, and 5-kb intervals from flanking regions were plotted.

(I) Heatmap analysis of ChIP-seq signals of *Rai1* peaks and H3K4me3, RNA pol2, Zfx, and GFP control signals. Peaks are ranked by *Rai1* peak intensity. See also [Figure S2](#).

enhanced splicing efficiency after Cre-mediated deletion of the preceding exon 3. Globally, RNA-seq showed that loss of *Rai1* caused changes in the expression levels of a small number of genes (Figure 3C), a subset of which were independently verified with qRT-PCR (Figure S3D). To further understand how *Rai1* regulates transcription, we combined the ChIP-seq and RNA-seq data obtained from the cortex. We found that *Rai1*-bound genes were globally downregulated in the *Nestin^{Cre};Rai1^{CKO}* brains; the fold changes were small but highly significant (Figure 3D). Therefore, *Rai1* appears to positively regulate expression of its direct targets. Genes upregulated in *Nestin^{Cre};Rai1^{CKO}* cortices are likely due to indirect effect of *Rai1* loss.

We further investigated how *Rai1* regulates transcription across developmental stages. The transcriptome of young mice may more closely reflect primary transcriptional changes due to loss of *Rai1*, whereas the adult tissue reflects a transcriptional state after prolonged *Rai1* dysfunction. We chose GABAergic neurons for this comparison as GABAergic spiny projection neurons represent 95% of all neurons within dorsal striatum, allowing us to remove *Rai1* in a relatively homogeneous population. qRT-PCR showed that *Rai1* exon 3 mRNA level in the *Gad2^{Cre};Rai1^{CKO}* dorsal striatum decreased by 80% in young (3-week-old) mice and 93% in adult (12-week-old) mice compared to sex- and age-matched control littermates (Figure S3E). We performed RNA-seq using dorsal striatum collected from 3- and 12-week-old control and *Gad2^{Cre};Rai1^{CKO}* mice. We found that most of the downregulated genes in the young mice remained downregulated in the adult stage, whereas many upregulated genes in the young mice became downregulated in the adult stage (Figure 3E). We also confirmed these expression patterns at both time points using qRT-PCR (Figures S3E and S3F). Therefore, genes are progressively downregulated in the *Rai1* mutant brain with age progression, supporting a general role for *Rai1* in positively regulating steady-state gene expression.

To gain insight into the biological processes regulated by *Rai1*, we compiled the downregulated genes identified from cortex and striatum (both young and adult) RNA-seq data (Table S5) and performed a gene ontology enrichment test. Functional annotation showed that *Rai1* regulates genes involved in cell adhesion, axon guidance, and neuronal morphogenesis (Figure 3F and Table S6), such as *Cdh7*, *Cdh8*, *Cdh9*, *Epha7*, *Pcdh20* (Figure S3G, left), and *Sema3a* (Figure S3G, right), suggesting that *Rai1* may help assemble and maintain neural circuits.

Pan-neural Knockout of *Rai1* Leads to Severe SMS-like Phenotypes

To explore the neural functions of *Rai1*, we next performed a battery of quantitative behavioral assays using the *Nestin^{Cre};Rai1^{CKO}* mice and their control littermates. It should be noted that although *Nestin^{Cre}* is expressed in progenitors that give rise to most or all neurons and glia in the CNS, it is also expressed in other organs (Harno et al., 2013; Tronche et al., 1999). The birth rate of *Nestin^{Cre};Rai1^{CKO}* mice conformed to a Mendelian ratio, suggesting that the embryonic lethality exhibited by *Rai1* null mice originates from *Nestin^{Cre}*-negative tissues. Due to occasional germline activity of *Nestin^{Cre}*, we also included mice produced in our breeding regime that lacked

one *Rai1* allele in their entire body (*Rai1^{Δ/+}* or *Rai1^{Δ/flox}*); these are the closest mouse models of SMS.

Nestin^{Cre};Rai1^{CKO} mice were smaller than littermates prior to weaning and showed prominent hindlimb claspings (Figure S4A). More than 80% of *Nestin^{Cre};Rai1^{CKO}* mice died before 25 weeks of age (Figure 4A). Most *Nestin^{Cre};Rai1^{CKO}* mice that died prior to 10 weeks of age were gaunt, exhibiting prominent kyphosis and demonstrated weight loss in the 2 weeks preceding death (Figure S4B). It has previously been reported that both SMS patients and *Rai1^{+/-}* mice are obese (Burns et al., 2010; Lacaria et al., 2012) and that female patients are more likely to exhibit food-seeking behavior than males (Edelman et al., 2007). In our experiments, only female *Nestin^{Cre};Rai1^{CKO}* mice became significantly overweight beginning at 5 weeks of age, while male mice were not affected (Figure 4B). The cause for the sexually dimorphic phenotype is unclear, and the interpretation could be complicated by weight loss prior to lethality in some mice. At 20 weeks of age, female *Nestin^{Cre};Rai1^{flox/+}* and *Nestin^{Cre};Rai1^{CKO}* mice became 35% and 101% heavier than control mice, respectively (Figure 4B). We thus used male *Nestin^{Cre};Rai1^{CKO}* mice for behavioral studies, so that behavioral assays would not be confounded by different body weights (Figure S4C).

First, we tested the motor function of *Nestin^{Cre};Rai1^{CKO}* mice. These mice displayed normal gait in the Catwalk assay (Figures S4D and S4E). In the activity chamber, the distance (Figures 4C and S4F) and zones (Figure S4G) traveled by *Nestin^{Cre};Rai1^{CKO}* mice were statistically indistinguishable from controls. The mean velocity and vertical activity (Figures S4H and S4I) was also normal. In the pole test, *Nestin^{Cre};Rai1^{CKO}* mice fell, slipped from the pole, or climbed down in a slow and uncoordinated fashion (Figure 4D). *Nestin^{Cre};Rai1^{CKO}* mice also showed decreased latency to fall in a wire hang test (Figure 4E). Interestingly, *Rai1^{+/-}* mice showed a decreased latency to fall, suggesting that performance in the wire hang test is more sensitive to *Rai1* dosage than the pole test.

Next, we examined whether the mice had deficits in tests purported to assess anxiety, sociability, and cognition. We measured anxiety-like behavior using the elevated plus maze and found that the time *Nestin^{Cre};Rai1^{CKO}* mice spent in open and closed arms was not statistically different from their control littermates (Figures S4J and S4K). Consistently *Nestin^{Cre};Rai1^{CKO}* and control mice exhibited no difference in exploring the periphery versus center in open field test (Figure S4G). *Nestin^{Cre};Rai1^{CKO}* mice also appeared normal in sociability and social discrimination assays (Figures S4L and S4M). However, *Nestin^{Cre};Rai1^{CKO}* mice exhibited a significantly reduced tendency to investigate the new arm in the Y-maze test (Figure S4N), suggesting a spatial working memory deficit.

Finally, in a Pavlovian fear-conditioning task that tests learning and memory, control mice progressively developed a freezing response to a tone followed by a shock, whereas *Nestin^{Cre};Rai1^{CKO}* mice had low freezing behavior after repeated tone-shock pairings during training (Figure 4F). As a result, these mice had reduced total freezing on the training day compared to littermates of other genotypes (Figure 4G). It is unlikely that these defects were caused by deficits in audition or pain sensation, as *Nestin^{Cre};Rai1^{CKO}* mice exhibited normal pain responses in the hot plate assay and normal auditory startle responses

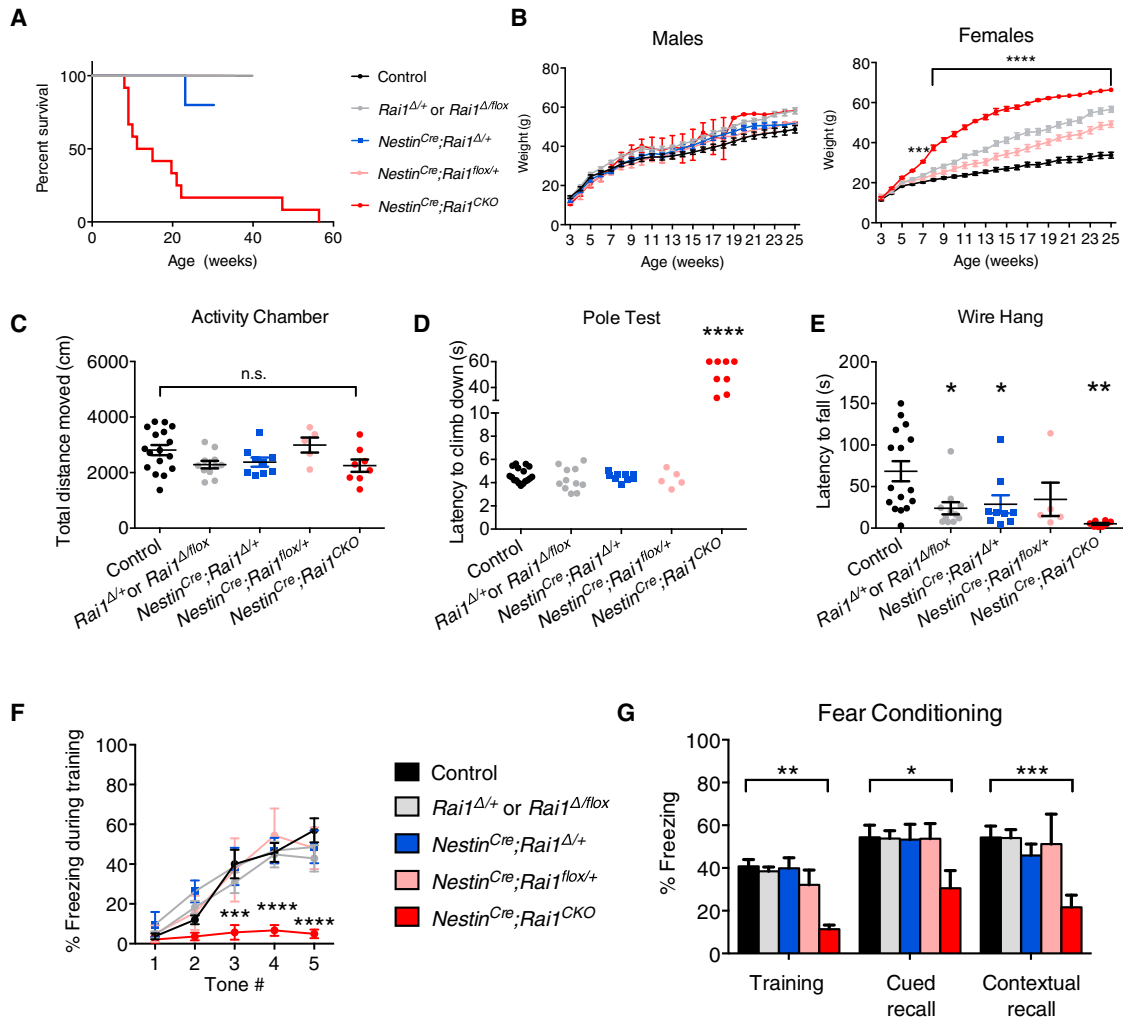


Figure 4. Pan-neural Loss of *Rai1* Causes SMS-like Phenotypes in Mice

(A) Survival curves for male and female control (*Rai1^{flox/+}*, *Rai1^{flox/flox}*, or *Nestin^{Cre/+}*, n = 26, black line), whole-body heterozygous knockout (*Rai1^{Δ/+}* or *Rai1^{Δ/flox}*, n = 27, gray line, overlaying the controls), whole-body heterozygous knockout plus *Nestin^{Cre}* (*Nestin^{Cre};Rai1^{Δ/+}*, n = 5, blue line), heterozygous *Nestin^{Cre}* knockout (*Nestin^{Cre};Rai1^{flox/+}*, n = 12, pink line, overlapped with controls), and homozygous *Nestin^{Cre}* knockout (*Nestin^{Cre};Rai1^{CKO}*, n = 12, red line) mice. Most *Nestin^{Cre};Rai1^{CKO}* mice die in early-to-mid adulthood, significantly younger than mice in all other groups (Log-rank test, p < 0.0001).

(B) Mean (±SEM) body weights over time of male (left) and female (right) control (n = 12 males and 16 females), *Rai1^{Δ/+}* or *Rai1^{Δ/flox}* (n = 11 males and 15 females), *Nestin^{Cre};Rai1^{Δ/+}* (n = 5 males and 0 females), *Nestin^{Cre};Rai1^{flox/+}* (n = 5 males and 7 females), and *Nestin^{Cre};Rai1^{CKO}* (n = 7 males and 5 females) mice. Female mice lacking one or both copies of *Rai1* in the *Nestin⁺* lineage or one copy in all tissues become obese (two-way ANOVA: genotype and genotype × time interaction, p < 0.001 for females and p > 0.05 for males).

(C) *Rai1* disruptions do not affect the distance traveled in an activity chamber. Each dot represents a single mouse. Data are mean ± SEM.

(D) Time (mean of three trials per mouse) required by each mouse to climb down a wooden pole after being placed at the top. Mice that fell or slipped off the pole were given a score of 60 seconds (s). *Nestin^{Cre};Rai1^{CKO}* mice slipped or fell down the pole, or climbed down very slowly, whereas heterozygous knockout and control mice agilely descended the pole in less than 6 s.

(E) Mean (±SEM) time mice were able to hang inverted from a wire grid before dropping; trials were terminated after 150 s (s), in which case mice were given scores of 150 s. *Rai1* heterozygous mice and *Nestin^{Cre};Rai1^{CKO}* mice show deficits in this task.

(F) Mean (±SEM) percentage time spent freezing during each tone on the training day of a trace fear-conditioning task. *Nestin^{Cre};Rai1^{CKO}* mice exhibit a drastic deficit in developing a freezing response compared to littermates of other genotypes.

(G) Mean (±SEM) percentage time spent freezing on all 3 days (training, cued recall, and contextual recall) of a trace fear-conditioning task. Values reflect total freezing with baseline period removed from the average.

Statistics: n.s., not significantly different, *p < 0.05, **p < 0.01, ***p < 0.001, and ****p < 0.0001, Tukey's post hoc test following a significant ANOVA.

See also Figure S4.

(data not shown). Also, the severe reduction of freezing behavior on the training day is unlikely to be caused by hyperactivity, as the *Nestin^{Cre};Rai1^{CKO}* mice exhibited normal locomotor activity

(Figures S4F–S4I). When the tone was presented by itself in a different context on the subsequent day (cued recall), *Nestin^{Cre};Rai1^{CKO}* mice exhibited more freezing compared to the training

day but still reduced compared to controls (Figure 4G). They also showed reduced freezing in the conditioning context without the tone (context recall) (Figure 4G). Therefore, despite modest steady-state transcriptomic changes, *Nestin^{Cre};Rai1^{CKO}* mice showed phenotypes that mimic many SMS symptoms, including deficits in body weight homeostasis, motor skills, and associative learning and memory.

Rai1 Loss in Subcortical Excitatory Neurons Causes Motor Dysfunction

As *Rai1* is widely expressed in the brain (Figure 1E), it is possible that (1) each phenotype is caused by loss of *Rai1* in a distinct group of cells (Figure 5A); (2) each cell type partially contributes to many phenotypes (Figure 5B); (3) most phenotypes are caused by loss of *Rai1* in one critical group of cells (Figure 5C); or a combination of the above. To distinguish between these possibilities, we selected three SMS-like phenotypes (motor, learning, and obesity) exhibited by *Nestin^{Cre};Rai1^{CKO}* mice and conducted a cell-type screen to determine whether loss of *Rai1* from specific cell populations would recapitulate these deficits. Specifically, one or both copies of *Rai1* was removed using (1) *Gad2^{Cre}* that targets most GABAergic inhibitory neurons (Taniguchi et al., 2011), (2) *Emx1^{Cre}* that targets cortical and hippocampal excitatory neurons and glia (Gorski et al., 2002), (3) *mGfap^{Cre}* that targets astrocytes and subsets of adult neural progenitors (Garcia et al., 2004), and (4) *Vglut2^{Cre}* that targets subcortical excitatory neurons (Vong et al., 2011). Immunostaining confirmed that *Rai1* was selectively deleted in Cre-expressing cells (Figures S5A–S5E; see Figure S6 for phenotypes other than motor, learning, and obesity analyzed in these conditional knockouts).

We first tested which cell types were responsible for the motor phenotypes seen in *Nestin^{Cre};Rai1^{CKO}* mice. All conditional mutants were similar in weight to their control littermates at the time of behavioral assays (Figure S5F). In the pole test, the time required to descend was increased only in *Vglut2^{Cre};Rai1^{CKO}* mice (Figures 5D–5G). In the wire hang test, *Gad2^{Cre};Rai1^{CKO}* mice performed slightly better than controls (Figure 5H), while removing one or both copies of *Rai1* from *Emx1⁺* or *mGfap⁺* cells did not interfere with performance (Figures 5I and 5J). By contrast, *Vglut2^{Cre};Rai1^{CKO}* mice developed poor motor functions, as exemplified by a decreased latency to fall in the wire hang test (Figure 5K). Removing one copy of *Rai1* from the *Vglut2⁺* neurons caused an intermediate phenotype in the wire hang test (Figure 5K). Thus, *Rai1* function in *Vglut2⁺* excitatory neurons is essential for proper motor function and is dosage sensitive in a subset of the assays.

Rai1 Loss in Either GABAergic Neurons or Subcortical Excitatory Neurons Disrupts Fear Conditioning

Fear conditioning is regulated by distributed networks in the brain involving excitatory and inhibitory neurons (Letzkus et al., 2015). We found that *Emx1^{Cre};Rai1^{CKO}* and *mGfap^{Cre};Rai1^{CKO}* mice did not show learning deficits (Figures 5M and 5N). However, both *Gad2^{Cre};Rai1^{CKO}* and *Vglut2^{Cre};Rai1^{CKO}* mice exhibited reduced freezing during training (Figures 5L and 5O). All conditional mutants and controls responded to shocks during training with increased locomotion or jumping, similar to control mice (data

not shown). Both *Gad2^{Cre};Rai1^{CKO}* and *Vglut2^{Cre};Rai1^{CKO}* mice exhibited normal pain sensitivity in a hot plate assay (Figure S5G), suggesting that the fear conditioning phenotypes were due to learning deficits rather than secondary consequences of defective pain sensitivity. Additionally, *Vglut2^{Cre};Rai1^{CKO}* and *Gad2^{Cre};Rai1^{CKO}* mice both showed reduced cued- and contextual-memory recall (Figures 5L and 5O), mimicking the *Nestin^{Cre};Rai1^{CKO}* mice. Together, these results indicate that *Rai1* is required in both *Gad2⁺* inhibitory and *Vglut2⁺* subcortical excitatory neurons for associative learning and memory.

Rai1 Loss in Subcortical Excitatory Neurons, Sim1⁺ Cells, or SF1⁺ Cells Causes Obesity

A prominent feature of SMS is truncal obesity, which develops in the young adolescent stage (Burns et al., 2010). Our analysis of *Nestin^{Cre};Rai1^{CKO}* mice suggested that *Rai1* levels in the nervous system significantly contributed to this deficiency, at least in females (Figure 4B). To identify the cell types responsible for obesity in *Rai1* mutant mice, we deleted *Rai1* using *Gad2^{Cre}*, *Emx1^{Cre}*, *mGfap^{Cre}*, and *Vglut2^{Cre}* lines. Only *Vglut2^{Cre};Rai1^{CKO}* mice showed increased body weight when compared to control littermates in both females (Figures 6A–6D) and males (Figures S7A–S7D). Unlike *Nestin^{Cre};Rai1^{CKO}* mice, *Vglut2^{Cre};Rai1^{CKO}* mice did not show premature lethality, and thus weight analysis did not suffer from the complication of weight loss prior to death, as in *Nestin^{Cre};Rai1^{CKO}* mice. Male and female *Vglut2^{Cre};Rai1^{CKO}* mice became obese at 9 and 7 weeks of age, respectively (Figures 6D and S7D) and were 56% (males) and 116% (females) heavier than control littermates at 20 weeks of age. Mice losing one copy of *Rai1* in the *Vglut2⁺* neurons were moderately overweight (males: 16% overweight, female: 29% overweight). By contrast, the body weight of *Emx1^{Cre};Rai1^{CKO}*, *Gad2^{Cre};Rai1^{CKO}*, and *mGfap^{Cre};Rai1^{CKO}* mice was not significantly different from their control littermates, highlighting that *Rai1* is specifically required for *Vglut2⁺* subcortical excitatory neurons to regulate energy homeostasis.

Next, we asked which subtypes of *Vglut2⁺* neurons regulate body weight. The hypothalamus is an important brain center for controlling appetite and energy expenditure (Saper and Lowell, 2014). Within the hypothalamus, *Vglut2^{Cre}* is expressed in the posterior hypothalamus, dorsal nucleus of hypothalamus, lateral hypothalamus, paraventricular nucleus of hypothalamus (PVH), ventromedial nucleus of hypothalamus (VMH), and a subset of POMC neurons in the arcuate nucleus (Vong et al., 2011). The VMH and PVH have emerged as critical hypothalamic nuclei that control feeding (Dhillon et al., 2006; Krashes et al., 2014). Therefore, we tested whether *Rai1* loss in PVH and/or the VMH would result in obesity.

In the hypothalamus, *Sim1^{Cre}* targets PVH (but not VMH) neurons, the majority of which are *Vglut2⁺* (Balthasar et al., 2005; Xu et al., 2013). *SF1^{Cre}* targets VMH (but not PVH) neurons, and the majority of VMH neurons targeted by *SF1^{Cre}* are also *Vglut2⁺* (Dhillon et al., 2006; Tong et al., 2007). We generated female *Sim1^{Cre};Rai1^{CKO}* and *SF1^{Cre};Rai1^{CKO}* mice, in which *Rai1* was preferentially deleted in the PVH or VMH, respectively, whereas in *Vglut2^{Cre};Rai1^{CKO}* mice *Rai1* was deleted from both nuclei (Figures S7E and S7F). Notably, *Sim1^{Cre};Rai1^{CKO}* mice were 57% heavier than their control littermates at 20 weeks of age

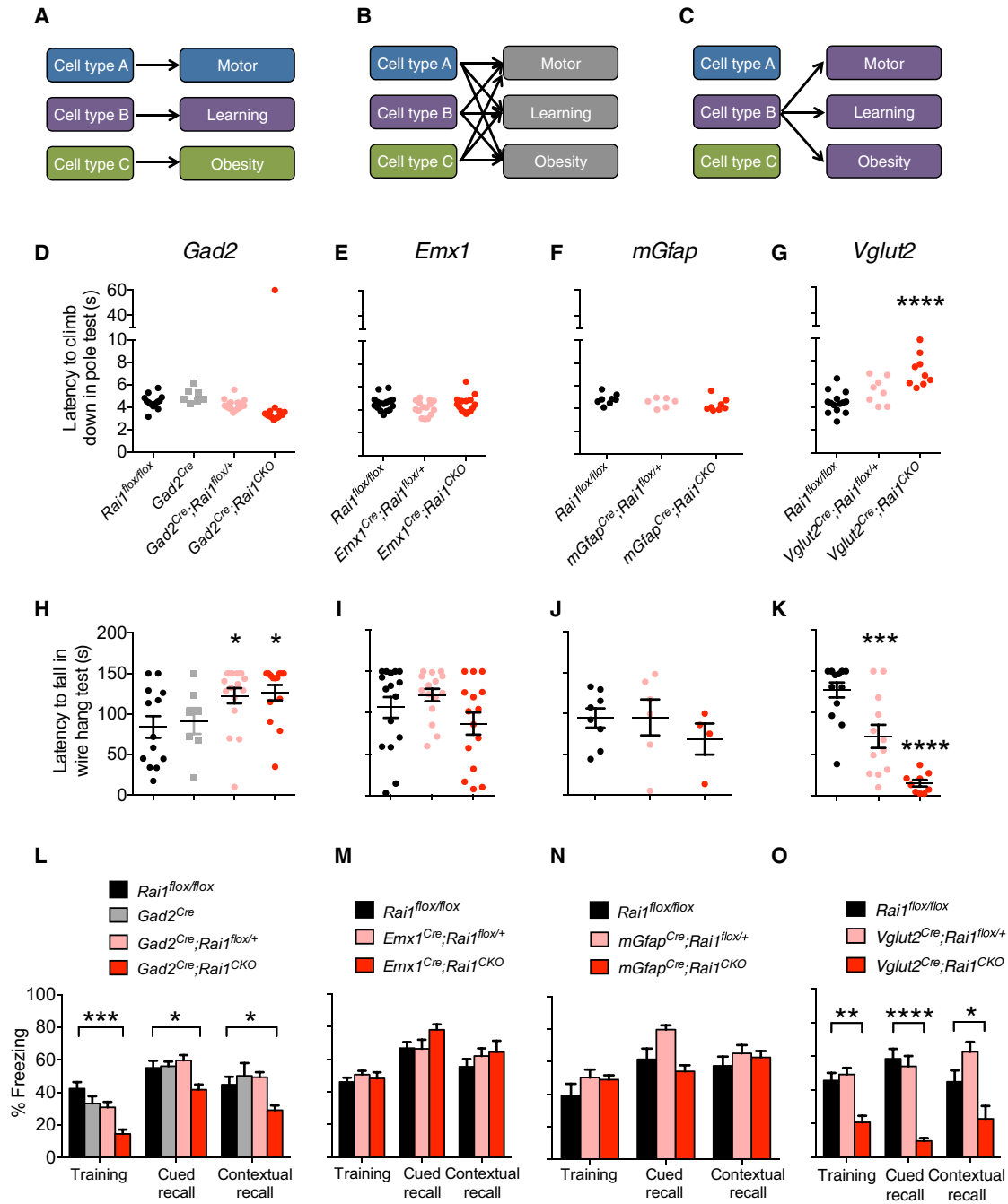


Figure 5. *Rai1* Is Required in Specific Neuronal Types for Motor Functions and Learning

(A–C) Three models for the relationship between *Rai1*'s function in specific cell types and its organismal functions. See text for details.

(D–K) Latency to descend in the pole test (D–G) and fall in the wire hang test (H–K) for mice in which *Rai1* was deleted in specific cell types as indicated. Data are mean ± SEM.

(L–O) Removal of *Rai1* in either *Gad2*⁺ (L) or *Vglut2*⁺ (O) neurons, but not in *Emx1*⁺ (M) or *mGfap*⁺ (N) cells, impairs performance in a fear-conditioning task. Data are mean ± SEM.

Statistics: **p* < 0.05, ***p* < 0.01, ****p* < 0.001, and *****p* < 0.0001, Tukey's post hoc test following a significant ANOVA.

See also Figures S5 and S6.

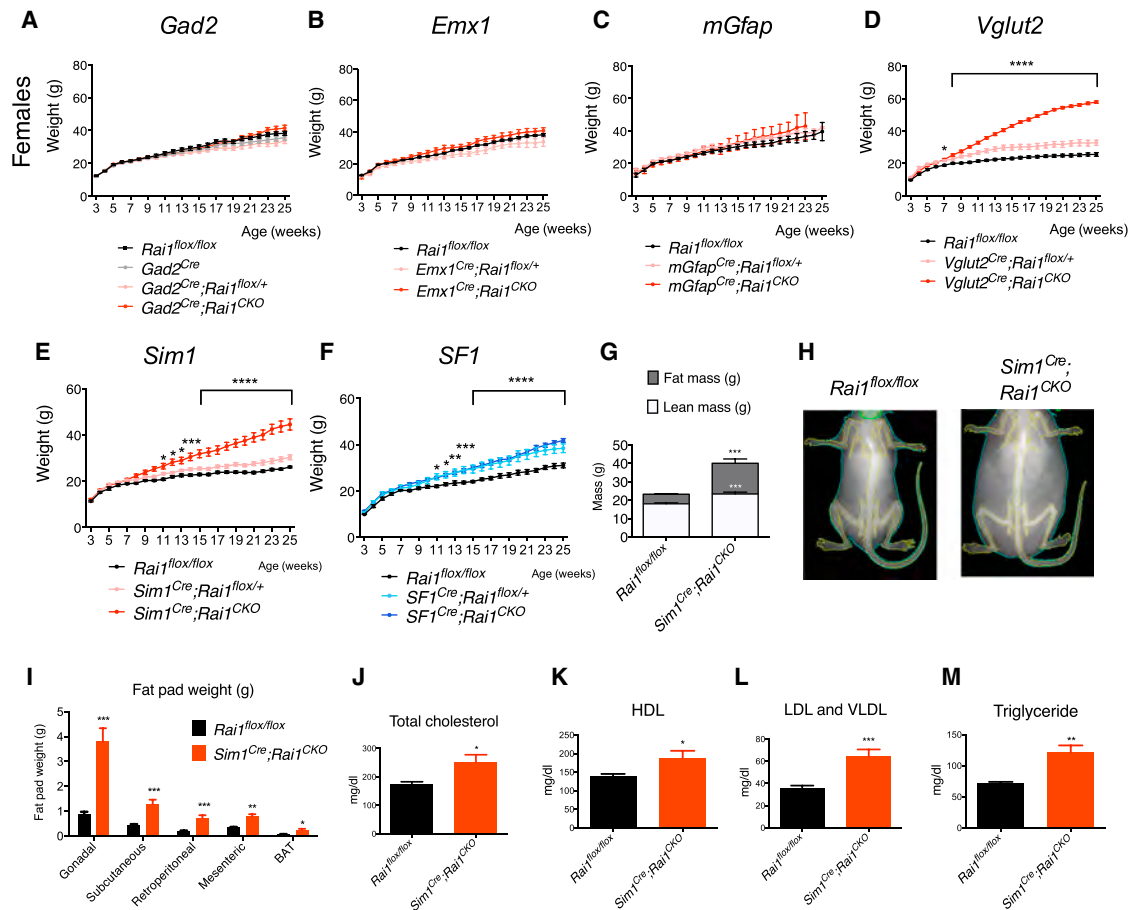


Figure 6. *Rai1* in *Vglut2*⁺ Neurons Controls Energy Homeostasis

(A–D) Mean (±SEM) body weights over time of female mice missing one or both copies of *Rai1* in the *Gad2* (A, n = 10–20 for each genotype), *Emx1* (B, n = 6–8 for each genotype), *mGfap* (C, n = 6–10 for each genotype), and *Vglut2* (D, n = 12–19 for each genotype)-Cre lineages. Female *Vglut2^{Cre}; Rai1^{flox/+}* and *Vglut2^{Cre}; Rai1^{CKO}* mice become significantly obese beginning at 9 and 7 weeks of age, respectively. For *Vglut2^{Cre}; Rai1^{flox/+}* mice: * at 9 weeks, ** at 10 weeks, *** at 11 and 12 weeks, **** at 13–25 weeks.

(E and F) Mean (±SEM) body weights over time of female mice missing one or both copies of *Rai1* in the *Sim1*⁺ (E, n = 10–13 for each genotype) or *SF1*⁺ (F, n = 8–16 for each genotype) neurons.

(G and H) Body composition (G, mean ± SEM) and representative images (H) of 30-week-old female *Rai1^{flox/flox}* and *Sim1^{Cre}; Rai1^{CKO}* mice as measured with dual-energy X-ray absorptiometry (n = 8 for each genotype).

(I) Fat pad weight (mean ± SEM) of 30-week-old female *Rai1^{flox/flox}* and *Sim1^{Cre}; Rai1^{CKO}* mice (n = 8 for each genotype).

(J–M) Serum levels (mean ± SEM) of total cholesterol (J), high-density lipoprotein (HDL) (K), low-density lipoprotein and very low-density lipoprotein (LDL and VLDL) (L), and triglyceride (M) in 30-week-old female *Rai1^{flox/flox}* and *Sim1^{Cre}; Rai1^{CKO}* mice (n = 8 for each genotype).

Statistics: *p < 0.05, **p < 0.01, ***p < 0.001, and ****p < 0.0001; Tukey's post hoc test following a significant ANOVA (A–F); unpaired t test (G–M).

See also [Figure S7](#).

([Figure 6E](#)), whereas *SF1^{Cre}; Rai1^{CKO}* mice were 27% heavier than controls at the same age ([Figure 6F](#)). Removing one copy of *Rai1* from the *Sim1*⁺ cells generated an intermediate overweight phenotype (12.7% heavier than controls at 20 weeks). Mice losing one copy of *Rai1* from the *SF1*⁺ cells were equally obese as *SF1^{Cre}; Rai1^{CKO}* mice, suggesting that *Sim1*⁺ and *SF1*⁺ cells are differentially sensitive to *Rai1* dosage. Therefore, both *Sim1*⁺ and *SF1*⁺ cells contribute to the obesity phenotype observed in *Vglut2^{Cre}; Rai1^{CKO}* mice, likely due to loss of *Rai1* in PVH and VMH neurons, respectively, although we cannot rule out the contribution of *Sim1*⁺ or *SF1*⁺ cells outside the PVH or VMH.

Given that *Sim1*⁺ cells played a more dominant role than *SF1*⁺ cells in obesity due to *Rai1* loss, we next aimed to identify the source of increased body weight in *Sim1^{Cre}; Rai1^{CKO}* mice. We quantified body composition with dual-energy X-ray absorptiometry (DEXA) and found that *Sim1^{Cre}; Rai1^{CKO}* mice showed significantly increased lean and fat mass ([Figures 6G](#) and [6H](#)). Consistent with DEXA results, the weight of each dissected fat pad, including brown adipose tissue (BAT), was greater in *Sim1^{Cre}; Rai1^{CKO}* mice ([Figure 6I](#)). These data indicate that *Sim1^{Cre}; Rai1^{CKO}* mice developed increased adiposity. In addition to obesity, SMS patients show higher levels of total cholesterol, HDL, LDL, and triglycerides ([Smith et al., 2002](#)). Consistent with

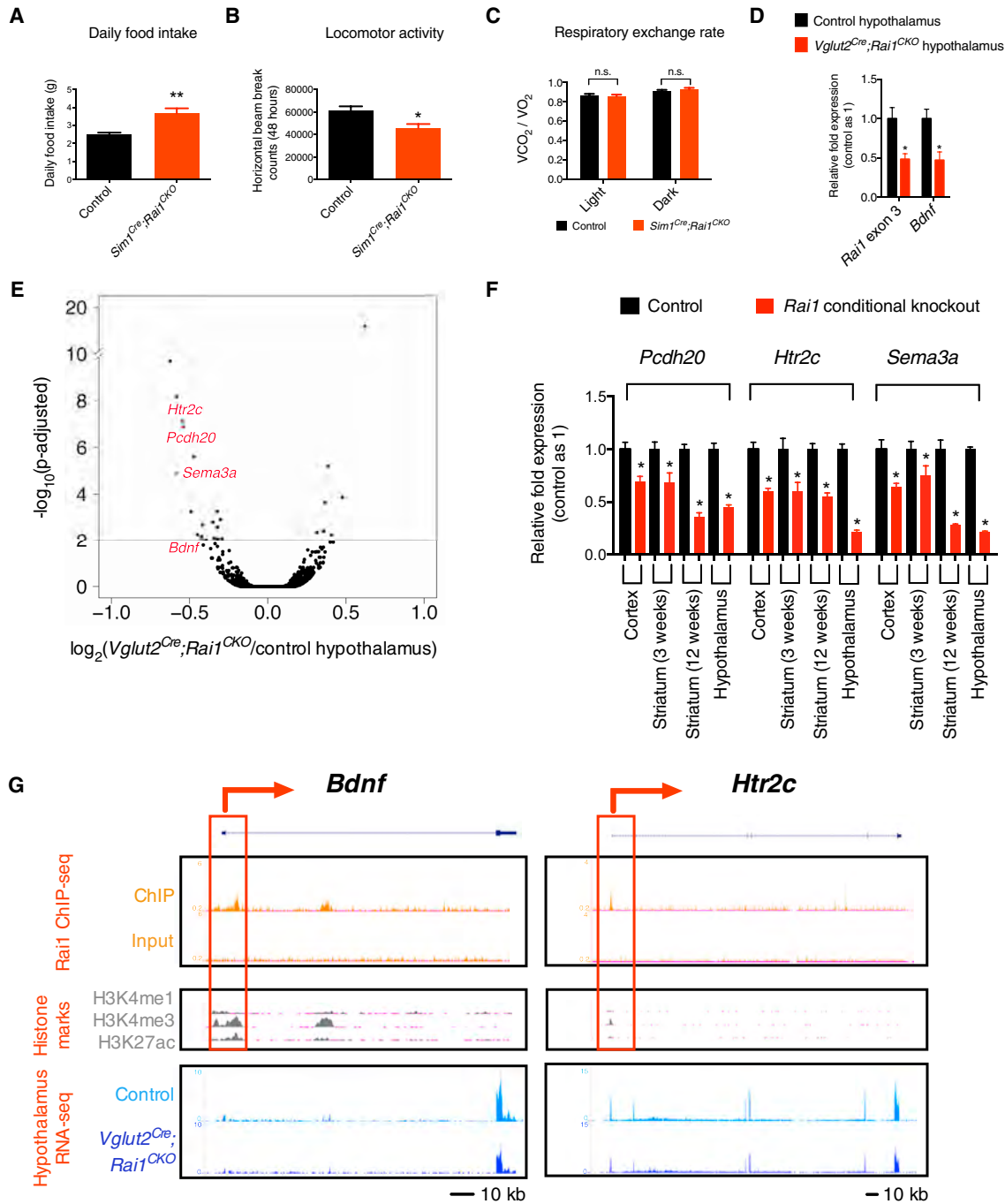


Figure 7. Mechanisms Underlying Hypothalamic Dysfunction upon *Rai1* Deletion

(A) Daily food intake of normal chow-fed mice (averaged over 7 days, mean \pm SEM). *Sim1^{Cre};Rai1^{CKO}* mice show significantly increased daily food intake (n = 8 for each genotype).

(B) Beam-break counts (mean \pm SEM) indicating a decrease of horizontal locomotor activity in 30-week-old *Sim1^{Cre};Rai1^{CKO}* mice (n = 8 for each genotype).

(C) Respiratory exchange rate (mean \pm SEM) as calculated by VCO_2/VO_2 is not significantly different among groups (n = 8 for each genotype).

(D) Expression of *Rai1* exon 3 and *Bdnf* are downregulated in the *Vglut2^{Cre};Rai1^{CKO}* hypothalamus, as revealed by qRT-PCR. Data are mean \pm SEM (n = 3).

(E) Volcano plot of RNA-seq results of control and *Vglut2^{Cre};Rai1^{CKO}* hypothalamus. Red dots indicate genes that were further validated.

(F) qRT-PCR showing that the mRNA expression of *Pcdh20*, *Htr2c*, and *Sema3a* are commonly downregulated in the *Nestin^{Cre};Rai1^{CKO}* cortex, *Gad2^{Cre};Rai1^{CKO}* striatum (both 3 weeks and 12 weeks), and *Vglut2^{Cre};Rai1^{CKO}* hypothalamus. Data are mean \pm SEM (n = 3).

(G) UCSC browser tracks of mouse *Bdnf* (left) and *Htr2c* (right) genomic loci annotated with *Rai1* ChIP-seq and input signals (orange, our data from cortex), histone marks (gray, ENCODE cortex data), and our RNA-seq signals from the control (light blue) and *Vglut2^{Cre};Rai1^{CKO}* (dark blue) hypothalamus. Red arrows

(legend continued on next page)

the human symptoms, *Sim1^{Cre};Rai1^{CKO}* mice exhibited similarly altered lipid profile (Figures 6J–6M). Finally, neither *Sim1^{Cre};Rai1^{CKO}* (Figure S7G) nor *SF1^{Cre};Rai1^{CKO}* (data not shown) pre-obese mice display a motor weakness in the wire hang test, suggesting that these neurons are not the *Rai1*-dependent *Vglut2⁺* subtypes that contribute to motor dysfunction.

Potential Mechanisms Underlying Obesity in *Rai1* Mutants

Obesity can be caused by increased food intake, decreased energy expenditure, or their combination. To distinguish among these possibilities in *Sim1^{Cre};Rai1^{CKO}* mice, we monitored their home cage food intake for a week. We found that they displayed hyperphagia, with a 47% increase in average daily food intake compared to control littermates (Figure 7A), and decreased horizontal locomotor activity over a 48 hr period (Figure 7B). Energy expenditure after normalization to lean body mass (Figures S7H–S7J) and respiratory exchange rate (Figure 7C) was not significantly affected. Together, these data suggest that hyperphagia may underlie the severe obesity in *Sim1^{Cre};Rai1^{CKO}* mice.

To identify the misregulated genes that may explain *Rai1*-associated obesity and increased food intake, we performed RNA-seq using hypothalamus isolated from *Vglut2^{Cre};Rai1^{CKO}* and control littermates at 8 weeks of age, before the conditional mutants became obese. *Rai1* mRNA was downregulated by ~50% in the *Vglut2^{Cre};Rai1^{CKO}* hypothalamus (Figure 7D), consistent with the fact that *Vglut2⁺* excitatory neurons only account for a subset of hypothalamic cells. Due to this dilution effect, and potential gene expression heterogeneity in *Vglut2⁺* neurons in different hypothalamic nuclei, the magnitude and number of differentially expressed genes in *Vglut2⁺* neurons are likely to be an underestimation. Still, we detected by RNA-seq (Figure 7E) and confirmed by qRT-PCR (Figure 7D) a previous observation that *Bdnf* is downregulated in *Rai1* heterozygous mice (Burns et al., 2010). In addition, we identified several genes involved in cell-cell communication, such as *Htr2c* (encoding the serotonin receptor 2c), *Pcdh20* (encoding a cell adhesion molecule protocadherin), and *Sema3a* (encoding an axon guidance protein), that were downregulated not only in *Vglut2^{Cre};Rai1^{CKO}* hypothalamus (Figure 7E), but also in the *Rai1* mutant cortex and striatum (Figure S3G and Table S5). We confirmed these downregulations independently by qRT-PCR (Figure 7F). Interestingly, both *Bdnf* and *Htr2c* mutant mice exhibit over-feeding behaviors that lead to obesity (Kernie et al., 2000; Tecott et al., 1995), and *Rai1* binds to the promoters of both *Bdnf* and *Htr2c* (Figure 7G). Together, our hypothalamus RNA-seq data suggest that decreased *Bdnf* and *Htr2c* expression due to *Rai1* loss may contribute to obesity.

DISCUSSION

Designing treatment strategies for neurodevelopmental disorders associated with genetic mutations requires a comprehen-

sive understanding of their genetic causes, molecular functions of the affected genes, and the cell types that underlie different symptoms (Kaiser and Feng, 2015; Mullins et al., 2016; Wells et al., 2016; Zoghbi and Bear, 2012). In this study, we present an extensive functional analysis of *Rai1*—a causal gene for two syndromic neurodevelopmental disorders (SMS and PTLS)—at molecular and behavioral levels. Our data show that *Rai1* is broadly expressed in postmitotic neurons and binds to promoter regions to positively regulate the expression of target genes, many of which function in circuit assembly and neuronal communication. Each SMS phenotype may be caused by loss of *Rai1* in multiple non-overlapping cell types (Figure 8). Our finding that *Vglut2⁺* subcortical excitatory neurons are major contributors of most phenotypes further highlights the importance of targeting these neurons for therapeutic intervention.

Our systematic conditional knockout analyses provide new insights into the neural functions of *Rai1*. First, different cell types are differentially sensitive to loss of *Rai1*. For example, we did not detect any phenotypes in fear conditioning (Figure 5) or social interactions (Figure S6) resulting from removal of *Rai1* from the *Emx1⁺* cells, which includes all excitatory neurons in the cortex and hippocampus, despite the prominent *Rai1* expression in those cells. This is not because *Emx1⁺* cells are not required in these behavioral tasks. For instance, it is well established that hippocampal function is required in contextual fear conditioning (Tovote et al., 2015), and social interactions engage frontal cortex (Barak and Feng, 2016). These data suggest that *Rai1* does not have a general, house-keeping function that is required for every cell type. Rather, *Rai1* has more specific roles in certain cell types.

Second, dosage sensitivity of *Rai1* differs for cell types and phenotypic assays. For example, for obesity, *Sim1⁺* cells exhibit at most a mild heterozygous phenotype, *SF1⁺* cells exhibit a heterozygous phenotype that is as severe as homozygous knockout, and *Vglut2⁺* neurons—which include both *Sim1⁺* and *SF1⁺* cells—exhibit an intermediate heterozygous phenotype. Within *Vglut2⁺* neurons, losing one copy of *Rai1* causes a motor defect in the wire hang test but not pole test. Further, *Vglut2⁺* and *Gad2⁺* neurons necessary for learning are only dysfunctional when both copies of *Rai1* were deleted. The lack of some phenotypes after losing one copy of *Rai1*, which more closely mimics the human syndrome, may be due to differences in physiology of mice and humans or due to insufficient sensitivity of assays in mice to mimic human conditions.

Third, *Rai1* function in multiple cell types contributes to SMS-like phenotypes in mice (Figure 8). Learning deficits originate from loss of *Rai1* in either *Vglut2⁺* or *Gad2⁺* neurons, and obesity likely results from a combination of *Rai1* deficiency in hypothalamic PVH and VMH neurons. Indeed, loss of *Rai1* in *Sim1⁺* and *SF1⁺* cells alone results in less severe weight gain than if *Rai1* is removed from all *Vglut2⁺* neurons, suggesting an involvement of additional cell types. *Rai1* loss in *Vglut2⁺* neurons causes

indicate direction of transcription. *Rai1* binds to the promoter region of *Bdnf* and *Htr2c* (red boxed areas), which colocalizes with H3K4me3. Loss of *Rai1* causes decreased *Bdnf* and *Htr2c* expression.

Statistics: n.s., not significant, $p > 0.05$, * $p < 0.05$, ** $p < 0.01$, unpaired t test.

See also Figure S7.

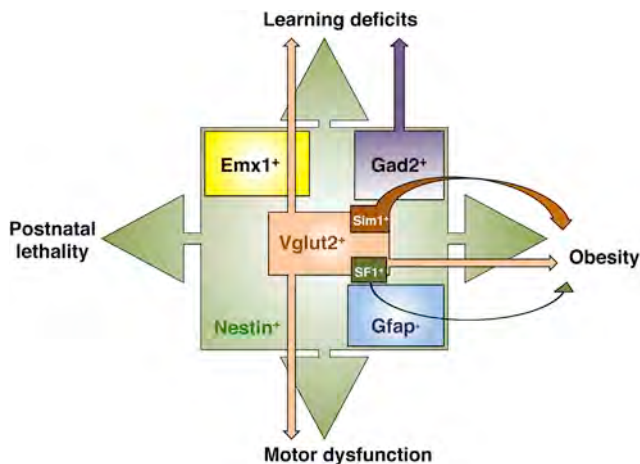


Figure 8. Cell-Type Specificity of SMS-like Phenotype in Mice

Schematic summary of the neurobehavioral phenotypes due to loss of *Rai1*, and the corresponding cell types that require *Rai1* identified in this study. Listed are four identified phenotypes observed in *Nestin^{Cre};Rai1^{CKO}* mice from our analyses. Whereas loss of *Rai1* in *Emx1⁺* and *Gfap⁺* cells does not lead to detectable phenotypes, *Rai1* function in these cell types can contribute to untested phenotypes or have additive/synergistic effects when combined with other cell types. *Rai1* loss in *Vglut2⁺* cells is a major contributor to learning, obesity, and motor phenotypes, and *Rai1* loss in *Gad2⁺* cells leads to learning deficits. *Rai1* in *Sim1⁺* cells, which include *Vglut2⁺* PVH neurons, is a dominant contributor to over-feeding and obesity phenotypes. *Rai1* in *SF1⁺* cells, including *Vglut2⁺* VMH neurons, plays a less prominent role in regulating body weight.

milder phenotypes than pan-neural *Rai1* loss in pole test for motor function, suggesting the involvement of additional cell types. Since removing *Rai1* from the subcortical *Vglut2⁺* but not cortical *Emx1⁺* glutamatergic neurons at least partially recapitulates many phenotypes seen in pan-neural *Rai1* knockout, our study uncovers a previously unappreciated involvement of subcortical excitatory neurons in SMS pathogenesis. Given that *Rai1* regulates a set of genes responsible for circuit assembly and neurotransmitter signaling, it will be interesting in the future to determine how loss of *Rai1* affects morphology and functions of subcortical excitatory neurons.

Monogenic models of neurodevelopmental disorders display a wide range of anatomical bases that account for their phenotypes. In tuberous sclerosis, conditional deletion of *Tsc1* in astrocytes, excitatory neurons, or inhibitory neurons all results in seizure in mice (Bateup et al., 2013; Fu et al., 2012; Uhlmann et al., 2002). In Rett syndrome, GABAergic neurons alone account for the majority of behavioral symptoms (Chao et al., 2010), with somatostatin- and parvalbumin-expressing interneurons each mediating non-overlapping Rett-like phenotypes (Ito-Ishida et al., 2015). Disrupted GABAergic signaling has been consistently demonstrated in neurodevelopmental disorders such as Rett syndrome, fragile X syndrome, *MECP2* duplication syndrome, and Dravet syndrome (Braat and Kooy, 2015). By comparison, the involvement of the subcortical glutamatergic system has not been as thoroughly studied. Our systematic analyses highlight the complex relationships between cell types and symptoms in SMS (Figure 8).

Given the strong phenotypes of *Rai1* mutant mice and the large number of *Rai1* binding sites in the genome revealed by our ChIP-seq analysis, loss of *Rai1* caused a surprisingly modest change in the transcriptome both in the number of genes and the magnitude of mRNA levels. One possible explanation is that besides moderately promoting gene expression, *Rai1* may regulate transcription in response to specific stimuli or changes in neuronal activity, which is not easily captured by sampling whole-tissue steady-state level of mRNAs. For example, several chromatin modifications have more important roles during dynamic gene activation and repression than steady-state expression (Weiner et al., 2012). Indeed, *Rai1*'s role in context-dependent transcription will be an interesting topic of future research. Another possible explanation is that misregulation of a small number of key *Rai1* target genes is sufficient to account for SMS symptoms. For example, we detected downregulation of *Bdnf* and *Htr2c* expression in *Vglut2^{Cre};Rai1^{CKO}* hypothalamus. Given the important roles for hypothalamic *Bdnf* (An et al., 2015; Xu and Xie, 2016) and *Htr2c* (Nonogaki et al., 1998; Tecott et al., 1995) in regulating energy homeostasis, the severe obesity observed in *Rai1* mutants may result from downregulation of one or both signaling pathways. In this regard, our study suggests an avenue for therapeutic intervention, at least for obesity, by restoring these signaling pathways. Given that there is an FDA-approved *Htr2c* agonist for treating obesity (Colman et al., 2012), this strategy can be tested experimentally.

EXPERIMENTAL PROCEDURES

Mouse Behavioral Assays

Male mice were housed in groups on an inverted 12/12 hr light/dark cycle with ad libitum access to food and water and were tested between 6 and 10 weeks of age. Behavioral testing was conducted during the mouse's subjective night, except the hot plate assay, which was performed during the subjective day. Mice were habituated to handling for 3 days prior to the onset of the first behavioral tests. Behavioral tests were conducted in multiple cohorts of mice; each cohort followed the same sequence of behavioral tests as listed in Supplemental Experimental Procedures. Experimenters were blind to mouse genotype during testing.

Detailed description of mouse behavioral assays, as well as additional methods are described in Supplemental Experimental Procedures, including mouse husbandry and handling, generation of the *Rai1-Tag* mice and *Rai1-flox* mice, mouse genotyping, protein expression and purification, in vitro binding assay, generation of *Rai1* antibody, in situ hybridization followed by immunostaining, immunostaining and antibodies, chromatin immunoprecipitation-sequencing (ChIP-seq) and ChIP-qPCR, RNA-seq and qRT-PCR, data analysis for ChIP-seq and RNA-seq, energy homeostasis analyses, and reagents and data sharing.

SUPPLEMENTAL INFORMATION

Supplemental Information includes Supplemental Experimental Procedures, seven figures, and nine tables and can be found with this article online at <http://dx.doi.org/10.1016/j.neuron.2016.09.019>.

AUTHOR CONTRIBUTIONS

W.-H.H., C.J.G., and L.L. designed the study. W.-H.H. and C.J.G. generated the mouse models, performed experiments, and analyzed data. J.X., W.-H.H., and H.Y.C. analyzed and interpreted the ChIP-seq and RNA-seq data. W.-H.H., C.J.G., T.N., and M.S. performed mouse behavioral studies and data analyses. L.A.S. performed in situ hybridization. A.W.W., and O.G.

helped design and provided reagents for the in vitro chromatin assay. W.-H.H. and L.L. wrote the paper, with contributions from all authors.

ACKNOWLEDGMENTS

We thank Dr. J. Lupski (Baylor College of Medicine) for *Rai1* cDNA constructs; Dr. B. Lowell (Beth Israel Deaconess Medical Center) for the *Sim1^{Cre}* mice; Stanford Transgenic Facility for generating the knockin and conditional knockout mice; UC Davis Mouse Metabolic Phenotyping Center for mouse metabolic profiling (UCD MMPC NIH grant DK092993); S. Zarate and K. DeLoach for technical assistance; K. Beier, L. DeNardo, L. Heckman, J. Lui, A. Shuster, B. Weissbourd, and W.H. Wong for helpful comments on the manuscript. This work was supported by grants from the Simons Foundation (SFARI Explorer Award 205270 and Research Award 345098) to L.L., NIH (P50-HG007735) to H.Y.C., and NIH (R01 GM079641) to O.G. W.-H.H. is a Howard Hughes Medical Institute Fellow of the Jane Coffin Childs Memorial Research Fund. A.W.W. was supported by NIH training grant (T32 GM007276). L.L. is a Howard Hughes Medical Institute Investigator. L.L. dedicates this study to his daughter Connie and other SMS patients, whose cheerful spirits in the face of their challenges are an inspiration.

Received: May 20, 2016

Revised: August 13, 2016

Accepted: September 9, 2016

Published: September 29, 2016

REFERENCES

- An, J.J., Liao, G.Y., Kinney, C.E., Sahibzada, N., and Xu, B. (2015). Discrete BDNF neurons in the paraventricular hypothalamus control feeding and energy expenditure. *Cell Metab.* **22**, 175–188.
- Balthasar, N., Dalgaard, L.T., Lee, C.E., Yu, J., Funahashi, H., Williams, T., Ferreira, M., Tang, V., McGovern, R.A., Kenny, C.D., et al. (2005). Divergence of melanocortin pathways in the control of food intake and energy expenditure. *Cell* **123**, 493–505.
- Barak, B., and Feng, G. (2016). Neurobiology of social behavior abnormalities in autism and Williams syndrome. *Nat. Neurosci.* **19**, 647–655.
- Bateup, H.S., Johnson, C.A., Deneff, C.L., Saulnier, J.L., Kornacker, K., and Sabatini, B.L. (2013). Excitatory/inhibitory synaptic imbalance leads to hippocampal hyperexcitability in mouse models of tuberous sclerosis. *Neuron* **78**, 510–522.
- Bi, W., Ohyama, T., Nakamura, H., Yan, J., Visvanathan, J., Justice, M.J., and Lupski, J.R. (2005). Inactivation of *Rai1* in mice recapitulates phenotypes observed in chromosome engineered mouse models for Smith-Magenis syndrome. *Hum. Mol. Genet.* **14**, 983–995.
- Bi, W., Yan, J., Shi, X., Yuva-Paylor, L.A., Antalffy, B.A., Goldman, A., Yoo, J.W., Noebels, J.L., Armstrong, D.L., Paylor, R., and Lupski, J.R. (2007). *Rai1* deficiency in mice causes learning impairment and motor dysfunction, whereas *Rai1* heterozygous mice display minimal behavioral phenotypes. *Hum. Mol. Genet.* **16**, 1802–1813.
- Braat, S., and Kooy, R.F. (2015). The GABA_A Receptor as a Therapeutic Target for Neurodevelopmental Disorders. *Neuron* **86**, 1119–1130.
- Burns, B., Schmidt, K., Williams, S.R., Kim, S., Girirajan, S., and Elsea, S.H. (2010). *Rai1* haploinsufficiency causes reduced *Bdnf* expression resulting in hyperphagia, obesity and altered fat distribution in mice and humans with no evidence of metabolic syndrome. *Hum. Mol. Genet.* **19**, 4026–4042.
- Chao, H.T., Chen, H., Samaco, R.C., Xue, M., Chahrour, M., Yoo, J., Neul, J.L., Gong, S., Lu, H.C., Heintz, N., et al. (2010). Dysfunction in GABA signalling mediates autism-like stereotypies and Rett syndrome phenotypes. *Nature* **468**, 263–269.
- Chen, X., Xu, H., Yuan, P., Fang, F., Huss, M., Vega, V.B., Wong, E., Orlov, Y.L., Zhang, W., Jiang, J., et al. (2008). Integration of external signaling pathways with the core transcriptional network in embryonic stem cells. *Cell* **133**, 1106–1117.
- Colman, E., Golden, J., Roberts, M., Egan, A., Weaver, J., and Rosebraugh, C. (2012). The FDA's assessment of two drugs for chronic weight management. *N. Engl. J. Med.* **367**, 1577–1579.
- Darvekar, S., Johnsen, S.S., Eriksen, A.B., Johansen, T., and Sjøttem, E. (2012). Identification of two independent nucleosome-binding domains in the transcriptional co-activator SPBP. *Biochem. J.* **442**, 65–75.
- Darvekar, S., Rekdal, C., Johansen, T., and Sjøttem, E. (2013). A phylogenetic study of SPBP and RAI1: evolutionary conservation of chromatin binding modules. *PLoS ONE* **8**, e78907.
- Dhillon, H., Zigman, J.M., Ye, C., Lee, C.E., McGovern, R.A., Tang, V., Kenny, C.D., Christiansen, L.M., White, R.D., Edelman, E.A., et al. (2006). Leptin directly activates SF1 neurons in the VMH, and this action by leptin is required for normal body-weight homeostasis. *Neuron* **49**, 191–203.
- Dubourg, C., Bonnet-Brilhault, F., Toutain, A., Mignot, C., Jacqueline, A., Dieux, A., Gérard, M., Beaumont-Epinette, M.P., Julia, S., Isidor, B., et al. (2014). Identification of Nine New RAI1-Truncating Mutations in Smith-Magenis Syndrome Patients without 17p11.2 Deletions. *Mol. Syndromol.* **5**, 57–64.
- Edelman, E.A., Girirajan, S., Finucane, B., Patel, P.I., Lupski, J.R., Smith, A.C., and Elsea, S.H. (2007). Gender, genotype, and phenotype differences in Smith-Magenis syndrome: a meta-analysis of 105 cases. *Clin. Genet.* **71**, 540–550.
- Elsea, S.H., and Girirajan, S. (2008). Smith-Magenis syndrome. *Eur. J. Hum. Genet.* **16**, 412–421.
- Ernst, J., and Kellis, M. (2012). ChromHMM: automating chromatin-state discovery and characterization. *Nat. Methods* **9**, 215–216.
- Fu, C., Cawthon, B., Clinkscales, W., Bruce, A., Winzenburger, P., and Ess, K.C. (2012). GABAergic interneuron development and function is modulated by the *Tsc1* gene. *Cereb. Cortex* **22**, 2111–2119.
- Garcia, A.D., Doan, N.B., Imura, T., Bush, T.G., and Sofroniew, M.V. (2004). GFAP-expressing progenitors are the principal source of constitutive neurogenesis in adult mouse forebrain. *Nat. Neurosci.* **7**, 1233–1241.
- Girirajan, S., Patel, N., Slager, R.E., Tokarz, M.E., Bucan, M., Wiley, J.L., and Elsea, S.H. (2008). How much is too much? Phenotypic consequences of *Rai1* overexpression in mice. *Eur. J. Hum. Genet.* **16**, 941–954.
- Gorski, J.A., Talley, T., Qiu, M., Puellas, L., Rubenstein, J.L., and Jones, K.R. (2002). Cortical excitatory neurons and glia, but not GABAergic neurons, are produced in the *Emx1*-expressing lineage. *J. Neurosci.* **22**, 6309–6314.
- Greenberg, F., Lewis, R.A., Potocki, L., Glaze, D., Parke, J., Killian, J., Murphy, M.A., Williamson, D., Brown, F., Dutton, R., et al. (1996). Multi-disciplinary clinical study of Smith-Magenis syndrome (deletion 17p11.2). *Am. J. Med. Genet.* **62**, 247–254.
- Harno, E., Cottrell, E.C., and White, A. (2013). Metabolic pitfalls of CNS Cre-based technology. *Cell Metab.* **18**, 21–28.
- Heinz, S., Benner, C., Spann, N., Bertolino, E., Lin, Y.C., Laslo, P., Cheng, J.X., Murre, C., Singh, H., and Glass, C.K. (2010). Simple combinations of lineage-determining transcription factors prime cis-regulatory elements required for macrophage and B cell identities. *Mol. Cell* **38**, 576–589.
- Ito-Ishida, A., Ure, K., Chen, H., Swann, J.W., and Zoghbi, H.Y. (2015). Loss of MeCP2 in Parvalbumin- and Somatostatin-Expressing Neurons in Mice Leads to Distinct Rett Syndrome-like Phenotypes. *Neuron* **88**, 651–658.
- Kaiser, T., and Feng, G. (2015). Modeling psychiatric disorders for developing effective treatments. *Nat. Med.* **21**, 979–988.
- Kernie, S.G., Liebl, D.J., and Parada, L.F. (2000). BDNF regulates eating behavior and locomotor activity in mice. *EMBO J.* **19**, 1290–1300.
- Kleine-Kohlbrecher, D., Christensen, J., Vandamme, J., Abarrategui, I., Bak, M., Tommerup, N., Shi, X., Gozani, O., Rappaport, J., Salcini, A.E., and Helin, K. (2010). A functional link between the histone demethylase PHF8 and the transcription factor ZNF711 in X-linked mental retardation. *Mol. Cell* **38**, 165–178.
- Krashes, M.J., Shah, B.P., Madara, J.C., Olson, D.P., Strohlic, D.E., Garfield, A.S., Vong, L., Pei, H., Watabe-Uchida, M., Uchida, N., et al. (2014). An excitatory paraventricular nucleus to AgRP neuron circuit that drives hunger. *Nature* **507**, 238–242.

- Lacaria, M., Saha, P., Potocki, L., Bi, W., Yan, J., Girirajan, S., Burns, B., Elsea, S., Walz, K., Chan, L., et al. (2012). A duplication CNV that conveys traits reciprocal to metabolic syndrome and protects against diet-induced obesity in mice and men. *PLoS Genet.* **8**, e1002713.
- Lacaria, M., Gu, W., and Lupski, J.R. (2013). Circadian abnormalities in mouse models of Smith-Magenis syndrome: evidence for involvement of *RAI1*. *Am. J. Med. Genet. A.* **161A**, 1561–1568.
- Letzkus, J.J., Wolff, S.B., and Lüthi, A. (2015). Disinhibition, a circuit mechanism for associative learning and memory. *Neuron* **88**, 264–276.
- Malhotra, D., and Sebat, J. (2012). CNVs: harbingers of a rare variant revolution in psychiatric genetics. *Cell* **148**, 1223–1241.
- Mullins, C., Fishell, G., and Tsien, R.W. (2016). Unifying views of autism spectrum disorders: a consideration of autoregulatory feedback loops. *Neuron* **89**, 1131–1156.
- Nonogaki, K., Strack, A.M., Dallman, M.F., and Tecott, L.H. (1998). Leptin-independent hyperphagia and type 2 diabetes in mice with a mutated serotonin 5-HT_{2C} receptor gene. *Nat. Med.* **4**, 1152–1156.
- Potocki, L., Chen, K.S., Park, S.S., Osterholm, D.E., Withers, M.A., Kimonis, V., Summers, A.M., Meschino, W.S., Anyane-Yebo, K., Kashork, C.D., et al. (2000). Molecular mechanism for duplication 17p11.2- the homologous recombination reciprocal of the Smith-Magenis microdeletion. *Nat. Genet.* **24**, 84–87.
- Potocki, L., Bi, W., Treadwell-Deering, D., Carvalho, C.M., Eifert, A., Friedman, E.M., Glaze, D., Krull, K., Lee, J.A., Lewis, R.A., et al. (2007). Characterization of Potocki-Lupski syndrome (dup(17)(p11.2p11.2)) and delineation of a dosage-sensitive critical interval that can convey an autism phenotype. *Am. J. Hum. Genet.* **80**, 633–649.
- Ramocki, M.B., and Zoghbi, H.Y. (2008). Failure of neuronal homeostasis results in common neuropsychiatric phenotypes. *Nature* **455**, 912–918.
- Saper, C.B., and Lowell, B.B. (2014). The hypothalamus. *Curr. Biol.* **24**, R1111–R1116.
- Slager, R.E., Newton, T.L., Vlangos, C.N., Finucane, B., and Elsea, S.H. (2003). Mutations in *RAI1* associated with Smith-Magenis syndrome. *Nat. Genet.* **33**, 466–468.
- Smith, A.C., McGavran, L., Robinson, J., Waldstein, G., Macfarlane, J., Zonona, J., Reiss, J., Lahr, M., Allen, L., and Magenis, E. (1986). Interstitial deletion of (17)(p11.2p11.2) in nine patients. *Am. J. Med. Genet.* **24**, 393–414.
- Smith, A.C.M., Boyd, K.E., Elsea, S.H., Finucane, B.M., Haas-Givler, B., Gropman, A., Laje, G., Magenis, E., and Potocki, L. (1993). Smith-Magenis Syndrome. In *GeneReviews(R)*, R.A. Pagon, M.P. Adam, H.H. Ardinger, S.E. Wallace, A. Amemiya, L.J.H. Bean, T.D. Bird, C.R. Dolan, C.T. Fong, R.J.H. Smith, and K. Stephens, eds. (Seattle: University of Washington), pp. 1993–2016.
- Smith, A.C., Gropman, A.L., Bailey-Wilson, J.E., Goker-Alpan, O., Elsea, S.H., Blancato, J., Lupski, J.R., and Potocki, L. (2002). Hypercholesterolemia in children with Smith-Magenis syndrome: del (17) (p11.2p11.2). *Genet. Med.* **4**, 118–125.
- Taniguchi, H., He, M., Wu, P., Kim, S., Paik, R., Sugino, K., Kvitsiani, D., Fu, Y., Lu, J., Lin, Y., et al. (2011). A resource of Cre driver lines for genetic targeting of GABAergic neurons in cerebral cortex. *Neuron* **71**, 995–1013.
- Tarpey, P.S., Smith, R., Pleasance, E., Whibley, A., Edkins, S., Hardy, C., O'Meara, S., Latimer, C., Dicks, E., Menzies, A., et al. (2009). A systematic, large-scale resequencing screen of X-chromosome coding exons in mental retardation. *Nat. Genet.* **41**, 535–543.
- Tecott, L.H., Sun, L.M., Akana, S.F., Strack, A.M., Lowenstein, D.H., Dallman, M.F., and Julius, D. (1995). Eating disorder and epilepsy in mice lacking 5-HT_{2c} serotonin receptors. *Nature* **374**, 542–546.
- Tong, Q., Ye, C., McCrimmon, R.J., Dhillon, H., Choi, B., Kramer, M.D., Yu, J., Yang, Z., Christiansen, L.M., Lee, C.E., et al. (2007). Synaptic glutamate release by ventromedial hypothalamic neurons is part of the neurocircuitry that prevents hypoglycemia. *Cell Metab.* **5**, 383–393.
- Tovote, P., Fadok, J.P., and Lüthi, A. (2015). Neuronal circuits for fear and anxiety. *Nat. Rev. Neurosci.* **16**, 317–331.
- Tronche, F., Kellendonk, C., Kretz, O., Gass, P., Anlag, K., Orban, P.C., Bock, R., Klein, R., and Schütz, G. (1999). Disruption of the glucocorticoid receptor gene in the nervous system results in reduced anxiety. *Nat. Genet.* **23**, 99–103.
- Uhlmann, E.J., Wong, M., Baldwin, R.L., Bajenaru, M.L., Onda, H., Kwiatkowski, D.J., Yamada, K., and Gutmann, D.H. (2002). Astrocyte-specific *TSC1* conditional knockout mice exhibit abnormal neuronal organization and seizures. *Ann. Neurol.* **52**, 285–296.
- Vong, L., Ye, C., Yang, Z., Choi, B., Chua, S., Jr., and Lowell, B.B. (2011). Leptin action on GABAergic neurons prevents obesity and reduces inhibitory tone to POMC neurons. *Neuron* **71**, 142–154.
- Weiner, A., Chen, H.V., Liu, C.L., Rahat, A., Klien, A., Soares, L., Gudipati, M., Pfeiffer, J., Regev, A., Buratowski, S., et al. (2012). Systematic dissection of roles for chromatin regulators in a yeast stress response. *PLoS Biol.* **10**, e1001369.
- Wells, M.F., Wimmer, R.D., Schmitt, L.I., Feng, G., and Halassa, M.M. (2016). Thalamic reticular impairment underlies attention deficit in *Ptchd1(Y-/-)* mice. *Nature* **532**, 58–63.
- Williams, S.R., Zies, D., Mullegama, S.V., Grotewiel, M.S., and Elsea, S.H. (2012). Smith-Magenis syndrome results in disruption of *CLOCK* gene transcription and reveals an integral role for *RAI1* in the maintenance of circadian rhythmicity. *Am. J. Hum. Genet.* **90**, 941–949.
- Xu, B., and Xie, X. (2016). Neurotrophic factor control of satiety and body weight. *Nat. Rev. Neurosci.* **17**, 282–292.
- Xu, Y., Wu, Z., Sun, H., Zhu, Y., Kim, E.R., Lowell, B.B., Arenkiel, B.R., Xu, Y., and Tong, Q. (2013). Glutamate mediates the function of melanocortin receptor 4 on *Sim1* neurons in body weight regulation. *Cell Metab.* **18**, 860–870.
- Zhang, F., Gu, W., Hurler, M.E., and Lupski, J.R. (2009). Copy number variation in human health, disease, and evolution. *Annu. Rev. Genomics Hum. Genet.* **10**, 451–481.
- Zhang, F., Potocki, L., Sampson, J.B., Liu, P., Sanchez-Valle, A., Robbins-Furman, P., Navarro, A.D., Wheeler, P.G., Spence, J.E., Brasington, C.K., et al. (2010). Identification of uncommon recurrent Potocki-Lupski syndrome-associated duplications and the distribution of rearrangement types and mechanisms in PTLs. *Am. J. Hum. Genet.* **86**, 462–470.
- Zoghbi, H.Y., and Bear, M.F. (2012). Synaptic dysfunction in neurodevelopmental disorders associated with autism and intellectual disabilities. *Cold Spring Harb. Perspect. Biol.* **4**, 4.

Neuron, Volume 92

Supplemental Information

Molecular and Neural Functions of *Rai1*, the Causal Gene for Smith-Magenis Syndrome

Wei-Hsiang Huang, Casey J. Guenther, Jin Xu, Tiffany Nguyen, Lindsay A. Schwarz, Alex W. Wilkinson, Or Gozani, Howard Y. Chang, Mehrdad Shamloo, and Liqun Luo

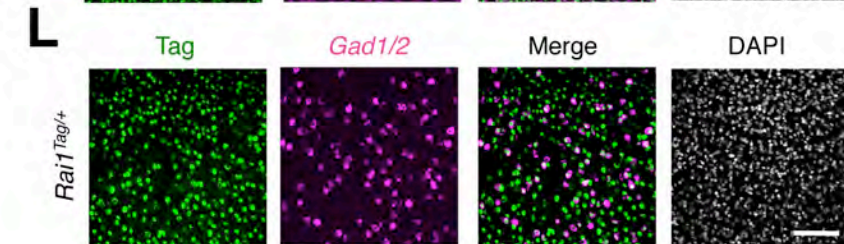
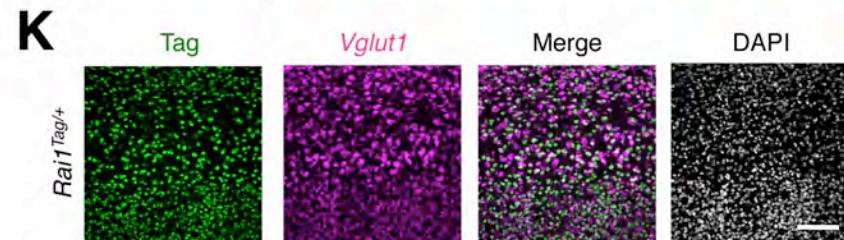
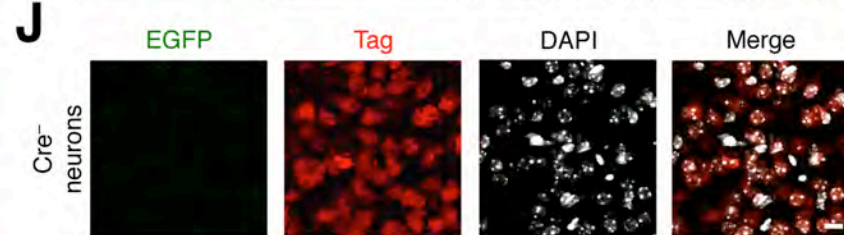
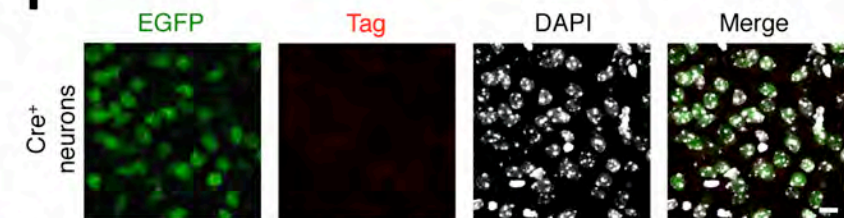
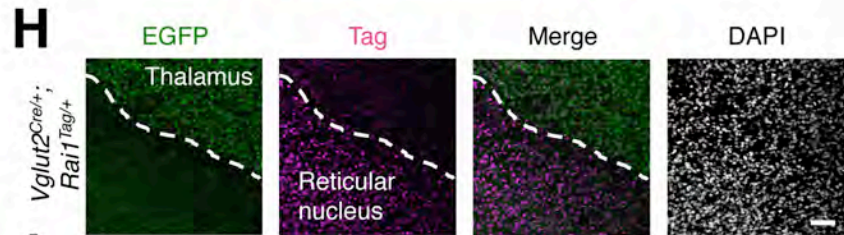
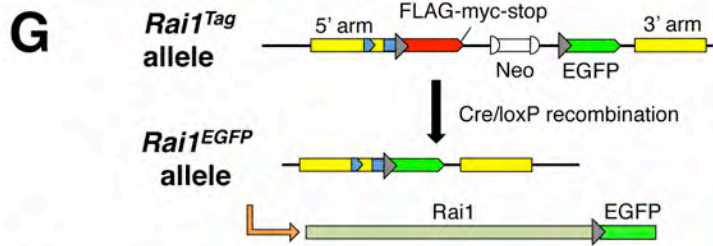
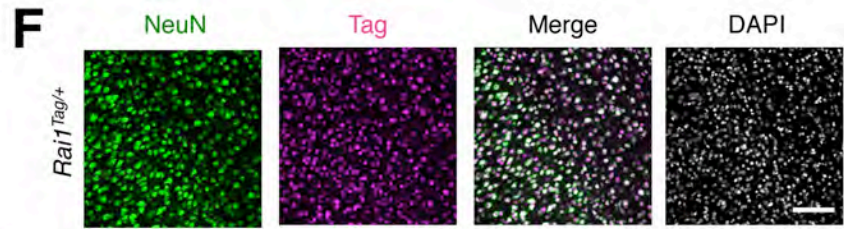
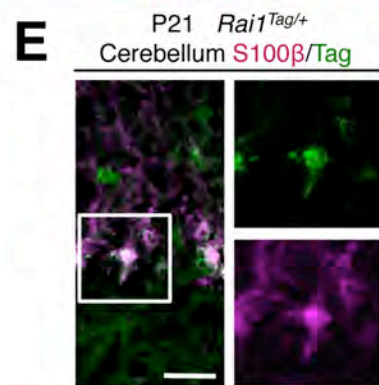
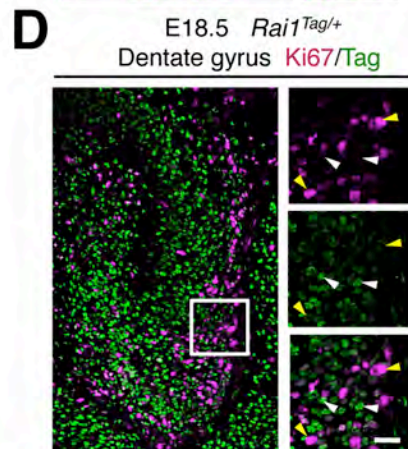
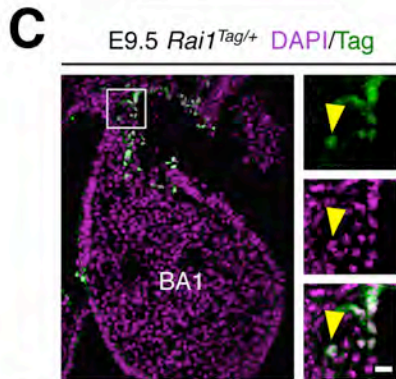
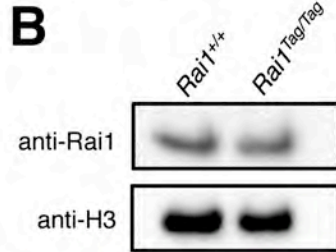
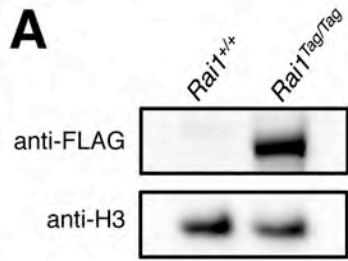


Figure S1. Characterizing Rai1 Expression Pattern Using Rai1-Tag, Related to Figure 1

(A) Western blot showing that anti-FLAG antibody detects Rai1-Tag fusion protein in *Rai1^{Tag/Tag}* but not wild-type (*Rai1^{+/+}*) mouse brains. Anti-histone H3 antibody serves as a loading control.

(B) Western blot using wild-type (*Rai1^{+/+}*) and *Rai1^{Tag/Tag}* mouse brains showing that the Tag peptide on the C terminus of Rai1 does not affect the expression of Rai1-Tag fusion protein, detected with an anti-endogenous Rai1 antibody. Anti-histone H3 antibody serves as a loading control.

(C) Sagittal section of an *Rai1^{Tag/+}* embryo showing that Tag-expressing cells (green, detected by anti-FLAG antibody) appeared in the first branchial arch (BA1) at E9.5. White box is magnified on the right, with yellow arrowheads pointing to an Rai1-Tag-expressing cell (green) that co-localizes with a DAPI⁺ nucleus (magenta). Scale bar: 10 μ m.

(D) Coronal section of an E18.5 *Rai1^{Tag/+}* hippocampus showing the expression pattern of Rai1-Tag (green). White box is magnified on the right, showing that Rai1-Tag and the mitotic marker Ki67 (magenta) do not overlap. Yellow arrowheads indicate Ki67⁺/Rai1⁻ cells, and white arrowheads indicate Ki67⁻/Rai1⁺ cells. Scale bar: 30 μ m.

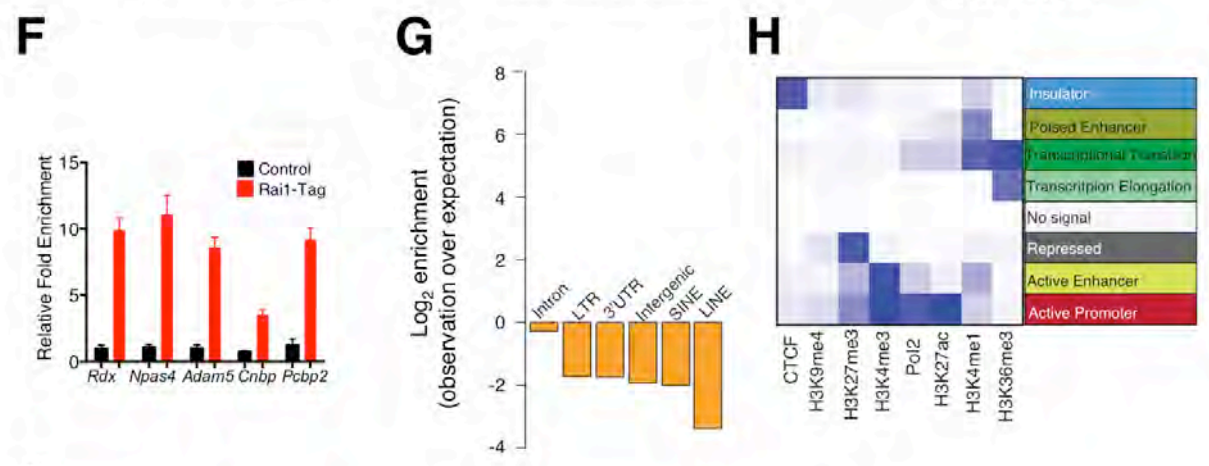
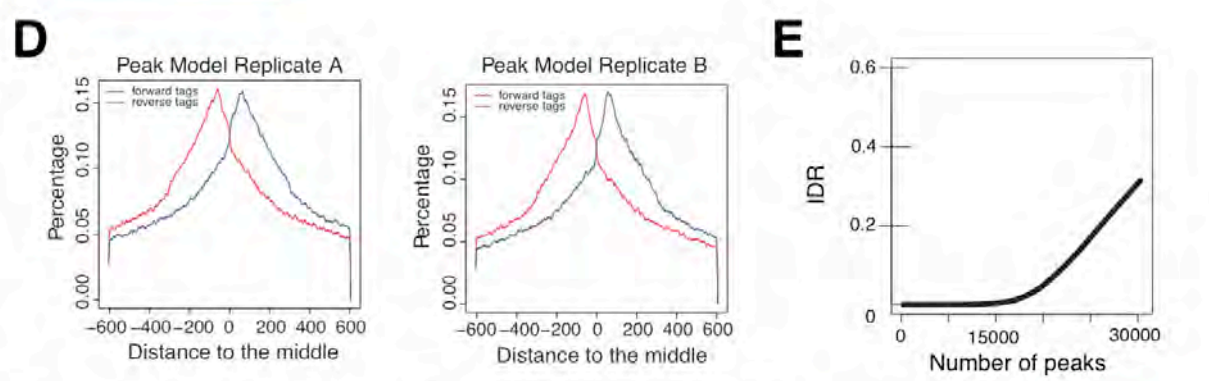
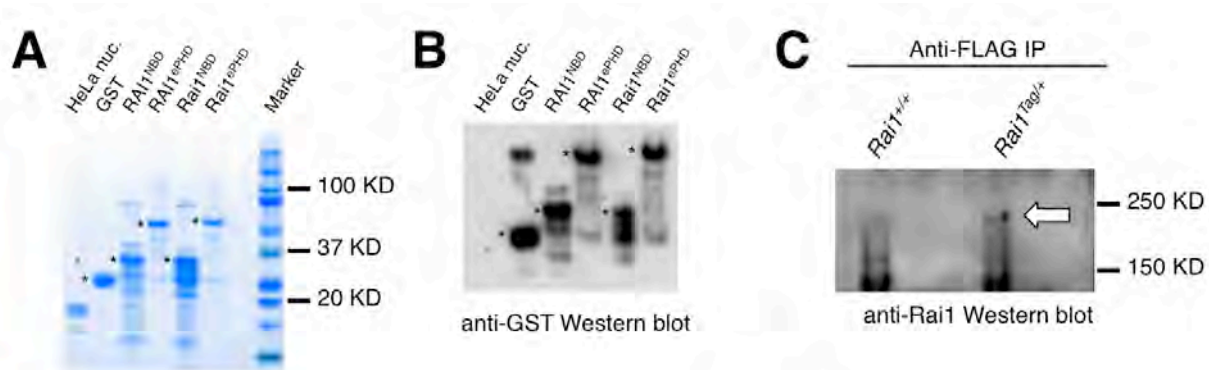
(E) Rai1 is occasionally detected in Bergmann glia in the cerebellar cortex, as Rai1-Tag (green) and a glial marker S100 β (magenta) are co-localized. White box is magnified on the right. Scale bar: 25 μ m.

(F) Co-staining of anti-myc antibody (magenta) showing that Rai1-Tag co-localizes with a pan-neuronal marker (NeuN, green). Scale bar: 100 μ m.

(G) The *Rai1^{Tag}* allele was designed to express an Rai1-enhanced green fluorescent protein (EGFP) fusion protein following Cre-mediated recombination. After Cre-mediated recombination, the Tag (red) and Neomycin (Neo) cassette were deleted, generating the *Rai1^{EGFP}* allele encoding an Rai1-EGFP fusion protein.

(H-J) Sagittal section of an E18.5 *Vglut2^{Cre/+}; Rai1^{Tag/+}* brain showing the Cre-positive thalamic neurons expressing Rai1-EGFP (detected by an anti-GFP antibody, green) abutting the Cre-negative reticular nucleus expressing Rai1-Tag (H). Dotted line indicates the boundary between the thalamus and reticular nucleus. The Cre-positive neurons express EGFP (green) but not Tag (red, detected by anti-myc antibody), indicating a successful Cre-dependent EGFP-tagging (I). The Cre-negative neurons express Rai1-Tag (red) but not EGFP (green), indicating that Rai1-EGFP expression is strictly Cre-dependent (J). Scale bars: (H): 50 μ m, (I-J): 10 μ m.

(K-L) In situ hybridization using a probe for *Vglut1* (K) and mixed probes for *Gad1/2* (L) followed by immunostaining using anti-myc antibody showing the co-localization between Rai1-Tag and neuronal subtype-specific markers. Scale bars: 100 μ m.



I

Rank	Motif	P-value	% of Targets	% of Background	Best Match
1		1.00E-58	44.68%	29.76%	ZNF711
2		1.00E-14	1.66%	0.39%	Foxo1
3		1.00E-13	11.95%	7.83%	Rfx4
4		1.00E-12	13.91%	9.62%	REST

Figure S2. Characterization of the Interaction Between Rai1 and Chromatin, Related to Figure 2

(A) SimplyBlue staining showing the protein integrity of HeLa nucleosome and recombinant GST-tagged proteins (*) used in nucleosome interaction assay.

(B) Western blot using an anti-GST antibody as a loading control for nucleosome interaction assay.

(C) Immunoprecipitation performed with anti-FLAG antibody using 8-week-old wild-type (*Rai1*^{+/+}, left lane) or *Rai1*^{Tag/+} cortex (right lane) followed by Western blot using an anti-Rai1 antibody. Rai1 is specifically pulled down from the *Rai1*^{Tag/+} but not wild-type cortex.

(D) Paired-end reads from CHIP-seq reveal that DNA fragments are equally likely to be sequenced from both ends. The tag density around a true binding site shows a bimodal enrichment pattern, with forward strand tags enriched upstream of binding and reverse strand tags enriched downstream. The bimodal enrichment was estimated by model-based analysis (MACS2). The two replicas show consistent bandwidth.

(E) Cumulative plot indicates the distribution of IDR (Irreproducible Discovery Rate), similar to False Discovery Rate (FDR), which controls the irreproducibility rate when selecting confidence peaks. The Y-axis indicates the IDR score (small value suggests high confidence in both replicas). The X-axis indicates the number of peaks that passed specific IDR scores on the Y-axis.

(F) ChIP-qPCR of control and *Rai1*^{Tag/+} brains using IgG and anti-flag antibodies. Input background was subtracted, and the fold enrichment (calculated as $2^{-\Delta\Delta C_t}$) of Rai1 was compared to negative control IgG (mean \pm SEM, n=3).

(G) Enrichment analysis showing genomic regions with less enriched Rai1 binding sites (orange) when compared to expected value, an extension of Figure 2D. LTR: long terminal repeat, SINE: short interspersed nuclear element, LINE: long interspersed nuclear element.

(H) Emission probability (left) of eight chromatin marks that divide the genome of the mouse cortex into eight chromatin states (right) (based on ChromHMM analysis), an extension of Figure 2F.

(I) Top significant enriched motifs in Rai1 binding regions identified by Homer motif analysis, an extension of Figure 2G. Shown are percentages of binding regions with motifs compared to random background and their respective p-values. The last column shows the best match for transcription factors with known similar motifs.

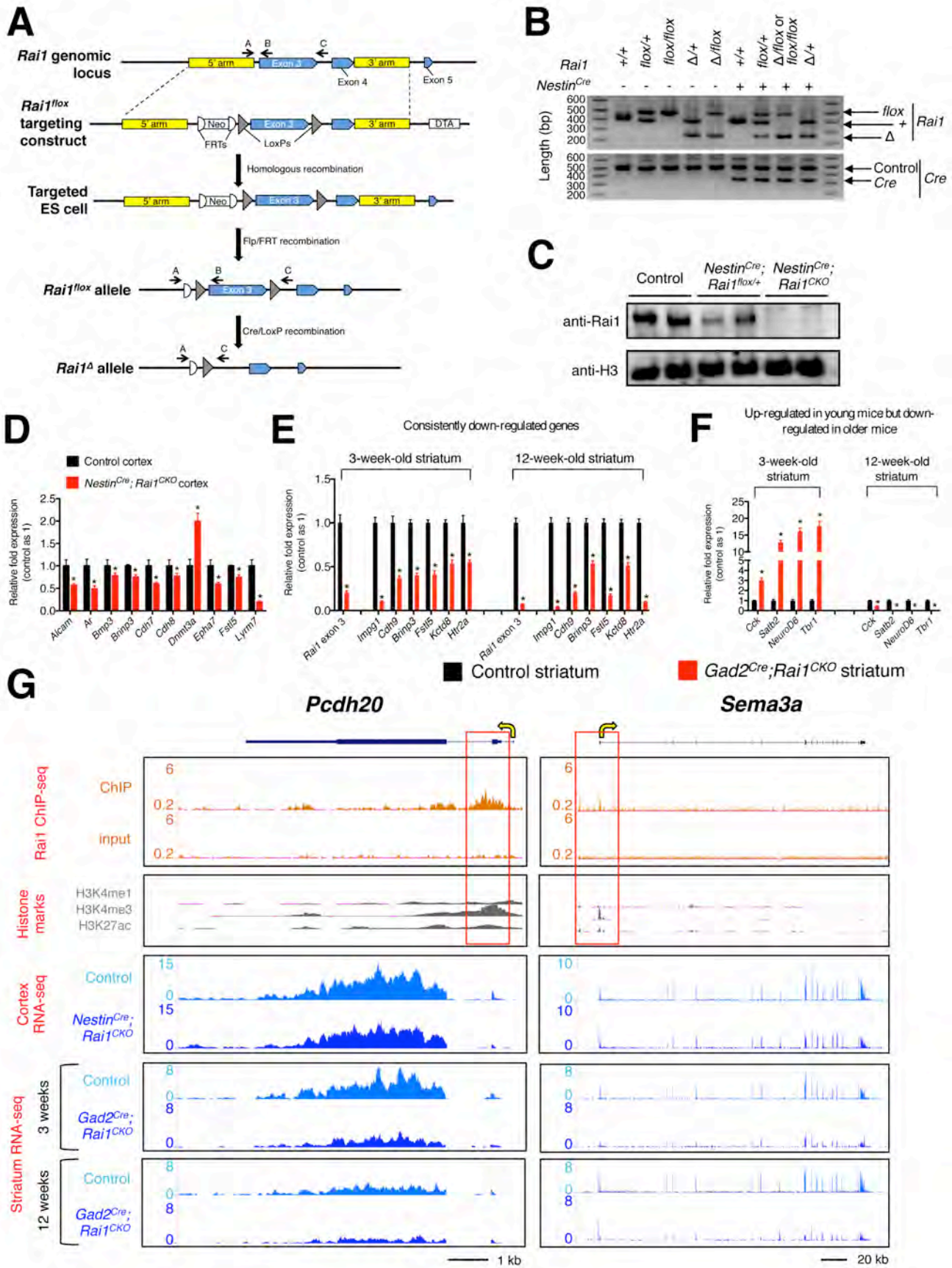


Figure S3. Generation of an *Rai1* Conditional Allele and *Rai1* Transcriptome Characterization, Related to Figures 1 and 3–7.

(A) The wild-type *Rai1* genomic locus (first row) is shown with yellow boxes indicating the 5' and 3' arms for homologous recombination. Blue boxes indicate the *Rai1* exons. ES cells were transfected with the *Rai1^{flox}* targeting construct (second row) to produce the post-targeted *Rai1* allele (third row). Chimeras were mated with a mouse line that expresses Flp recombinase in the germline to generate the *Rai1^{flox}* allele (fourth row). After Cre-mediated recombination, the largest exon (exon 3) that encodes amino acid 1–1837 of *Rai1* is deleted, generating an *Rai1^Δ* allele (fifth row). Neomycin (Neo) and diphtheria toxin A (DTA) cassettes were used for ES cell positive and negative selection, respectively. PCR primers A, B, and C were used for genotyping.

(B) Representative genotyping PCR products of the offspring of a *Nestin^{Cre};Rai1^{flox/+}* x *Rai1^{flox/+}* mating. PCRs were performed using primers that distinguish between different *Rai1* genotypes (top) and primers that detect *Nestin^{Cre}* (bottom). Each lane represents an individual animal, with the genotype of the animal indicated above. *Nestin^{Cre}* was detected using generic Cre primers that produce a band of ~300-bp in the presence of Cre. *Rai1* alleles were distinguished using primers A, B, and C, which produce a 396-bp band (primers A and B) from the wild-type *Rai1* allele (*Rai1⁺*), a 497-bp band (primers A and B) from the floxed *Rai1* allele (*Rai1^{flox}*), and a 261-bp band (primers A and C) from the *Rai1* null allele (*Rai1^Δ*). The product of primers A and C is too long to be efficiently amplified in wild-type or floxed alleles under the PCR conditions used. *Nestin^{Cre}* has occasional germline activity, so matings of *Nestin^{Cre}* and *Rai1^{flox}* mice produce some offspring that are heterozygous for *Rai1* throughout their entire bodies (*Rai1^{Δ/+}* and *Rai1^{Δ/flox}*). *Nestin^{Cre}* is also active in at least some tissues in the tail, so the *Rai1^Δ* allele can be detected in *Rai1^{flox/+}* and *Rai1^{flox/flox}* mice when *Nestin^{Cre}* is present. As a result, *Nestin^{Cre};Rai1^{flox/flox}* and *Nestin^{Cre};Rai1^{Δ/flox}* mice cannot be distinguished using this genotyping strategy.

(C) Western blot showing that the endogenous *Rai1* protein level is decreased in a dose-dependent manner in control (*Rai1^{flox/flox}*), *Nestin^{Cre};Rai1^{flox/+}*, and *Nestin^{Cre};Rai1^{CKO}* cortices. Two mice from each genotype are shown. Histone H3 serves as a loading control.

(D) Quantitative RT-PCR showing differentially expressed genes in the 3-week-old *Nestin^{Cre};Rai1^{CKO}* cortex, confirming RNA-seq results. Data are means ± SEM (*p < 0.05, unpaired t-test, n = 3).

(E) Quantitative RT-PCR of genes consistently down-regulated at different postnatal stages in the *Gad2^{Cre};Rai1^{CKO}* striatum (red bars) compared to controls (black bars). The expression of loxP-flanked *Rai1* exon 3 is down-regulated in the conditional mutants, confirming that *Gad2^{Cre}* efficiently removes *Rai1* from the dorsal striatum. Data are mean ± SEM (*p < 0.05, unpaired t-test, n = 3).

(F) Quantitative RT-PCR showing genes that are up-regulated in the young *Gad2^{Cre};Rai1^{CKO}* striatum (left) that become down-regulated in the older *Gad2^{Cre};Rai1^{CKO}* striatum (right). Data are means ± SEM (*p < 0.05, unpaired t-test, n = 3).

(G) UCSC genome browser view of *Pcdh20* (left) and *Sema3a* (right) loci. Yellow arrows indicate direction of transcription. Red boxed areas show that the promoter regions of *Pcdh20* and *Sema3a* are enriched with *Rai1* binding and the H3K4me3 mark. RNA-seq data for the cortex (3-week-old) and striatum (3- and 12-week-old) are shown below. *Pcdh20* and *Sema3a* expression are decreased in *Rai1* deficient tissues.

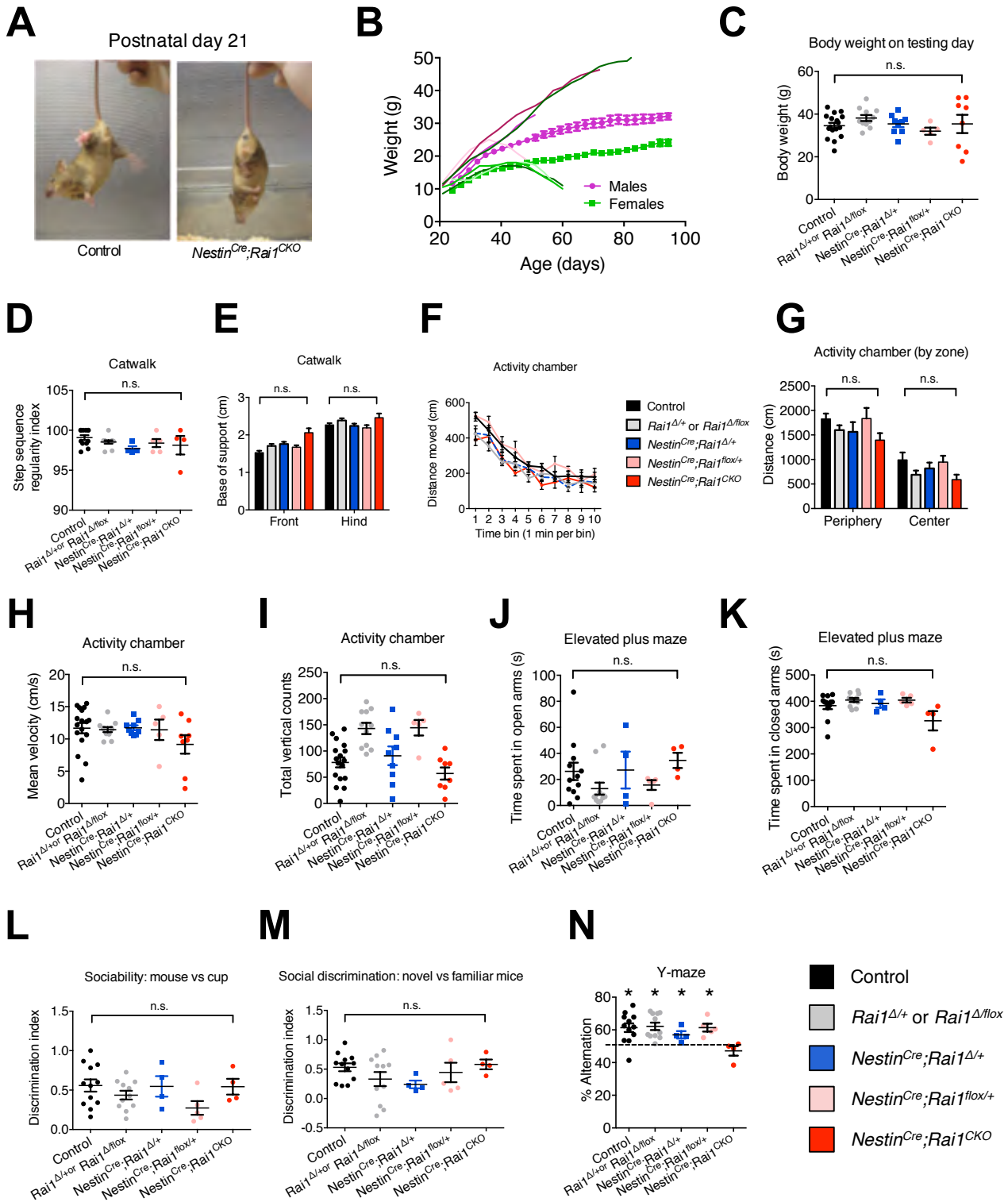


Figure S4. Behavioral Characterization of the *Nestin^{Cre};Rai1^{CKO}* Mice, Related to Figure 4

(A) Representative of the hindlimb clasping phenotype of a *Nestin^{Cre};Rai1^{CKO}* mouse.

(B) Representative weights of individual males and females (magenta and green lines with different shades, respectively) of *Nestin^{Cre};Rai1^{CKO}* mice prior to death (lines without points) and mean weights (\pm SEM) of control mice (squares and circles, n=13 for males, n=12 for females). Most *Nestin^{Cre};Rai1^{CKO}* mice gained weight normally immediately following weaning but lost weight in the two weeks prior to death.

(C) The body weights (mean \pm SEM) of male *Nestin^{Cre};Rai1^{CKO}* mice are not significantly different from control mice during behavioral analyses. Phenotypes across groups were analyzed by one-way ANOVA unless otherwise stated. n.s., not significantly different.

(D-E) Gait parameters, including step sequence (D) and base of support (E), are normal for *Nestin^{Cre};Rai1^{CKO}* mice in the Catwalk assay (mean with SEM).

(F-I) In the activity chamber, *Nestin^{Cre};Rai1^{CKO}* mice do not differ from controls in the distance moved over time (F), time spent in the periphery versus center of the chamber (G), mean velocity (H), and vertical activity (I) (mean with SEM).

(J-K) Time (mean \pm SEM) spent in the open (J) and closed (K) arms of an elevated plus maze do not differ between *Nestin^{Cre};Rai1^{CKO}* mice and controls.

(L) *Nestin^{Cre};Rai1^{CKO}* mice, similar to the controls, show a higher interest towards a mouse versus a cup (mean \pm SEM, paired t-test), as calculated by discrimination index (see Supplemental Experimental Procedures).

(M) The ability to discriminate a novel versus familiar mouse, as calculated by discrimination index, is statistically indistinguishable between *Nestin^{Cre};Rai1^{CKO}* and control mice (mean \pm SEM).

(N) Alternation between arms of a Y-Maze is reduced in *Nestin^{Cre};Rai1^{CKO}* mice. Shown are mean \pm SEM. One sample t-test to a hypothetical mean of 50% (* p < 0.05).

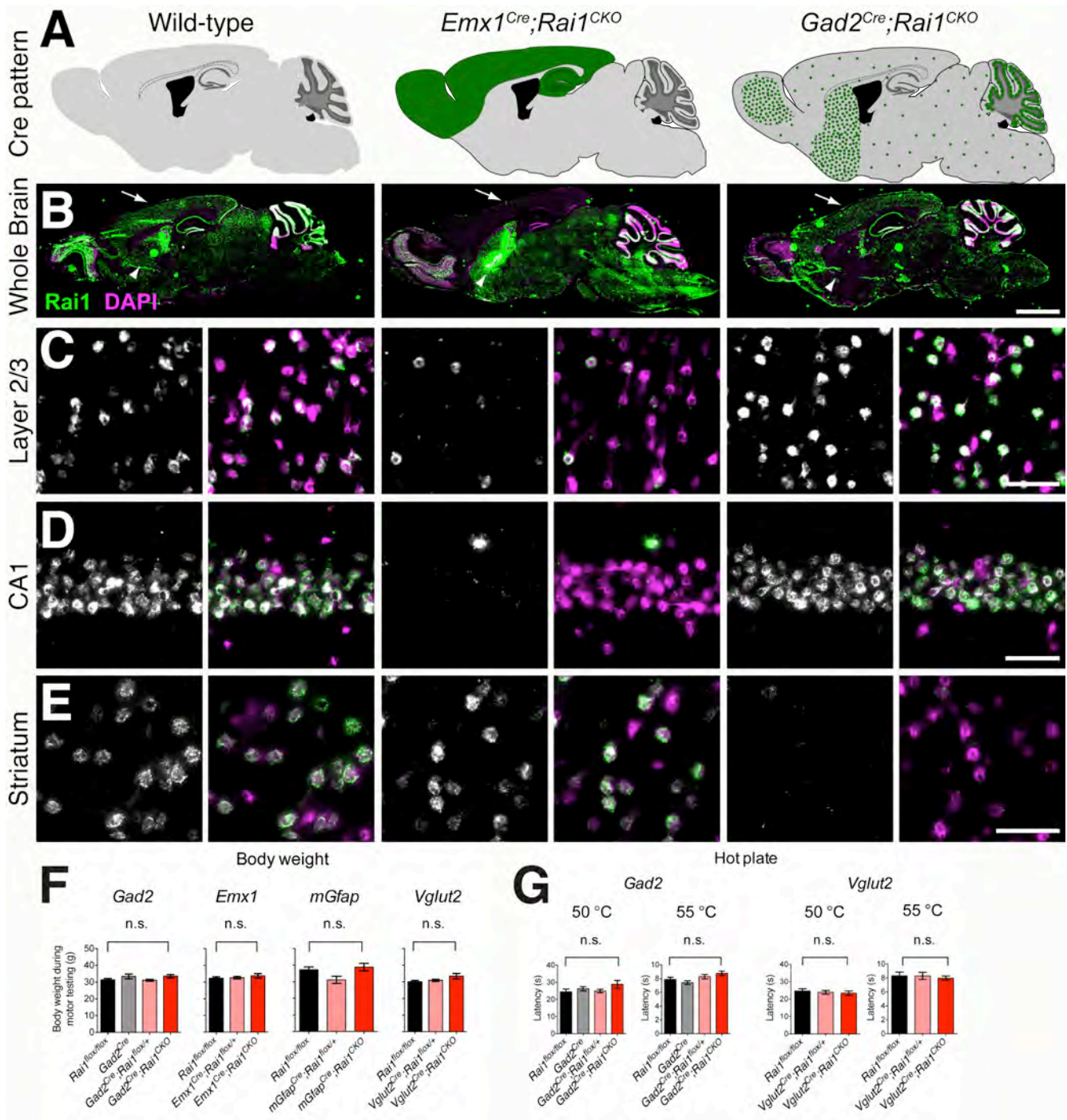


Figure S5. Characterization of *Rai1* Conditional Mutants, Related to Figure 5

(A) Schematic parasagittal adult brain sections showing the regions (in green) targeted by *Emx1^{Cre}* (middle) and *Gad2^{Cre}* (right). *Emx1^{Cre}* predominantly targets excitatory neurons in the cortex and hippocampus, along with a fraction of cells in the olfactory bulb. *Gad2^{Cre}* targets inhibitory neurons throughout the brain.

(B) Representative images of parasagittal whole brain sections for the above three genotypes stained with an anti-Rai1 antibody (green) and DAPI (magenta). Rai1 signal is greatly reduced in the cortex (arrows) of *Emx1^{Cre};Rai1^{CKO}* compared with wild-type and *Gad2^{Cre};Rai1^{CKO}* mice, consistent with most cortical neurons being *Emx1⁺*. Rai1 signal is greatly reduced in the striatum (arrowheads) of *Gad2^{Cre};Rai1^{CKO}* compared with wild-type and *Emx1^{Cre};Rai1^{CKO}* mice, consistent with most striatal neurons being *Gad2⁺*. Scale bars: 2 mm.

(C-E) High magnification images of layer 2/3 of primary somatosensory cortex (C), CA1 region of the hippocampus (D), and the striatum (E) immunostained with an anti-Rai1 antibody and DAPI. The left column is anti-Rai1 immunostaining alone (white), and the right column is anti-Rai1 immunostaining (green) merged with DAPI (magenta, co-localization shown in white). In *Emx1^{Cre};Rai1^{CKO}* mice, Rai1 is absent in most cells of the cortex (C) and hippocampus (D), while in *Gad2^{Cre};Rai1^{CKO}* mice, Rai1 is absent in most cells of the striatum (E). Scale bars: 100 μ m (C), 40 μ m (D-E).

(F) Mean body weights (mean \pm SEM) of different male *Rai1* conditional mutant mice are indistinguishable from *Rai1^{flox/flox}* mice during motor function testing. n.s., not significantly different, one-way ANOVA.

(G) The latency (mean \pm SEM) to paw licking or jumping for escape after being placed on either a 50°C (left) or 55°C (right) hot plate do not differ for *Gad2^{Cre};Rai1^{CKO}* and *Vglut2^{Cre};Rai1^{CKO}* mice with *Rai1^{flox/flox}* mice, suggesting a normal analgesic response. n.s., not significantly different, one-way ANOVA.

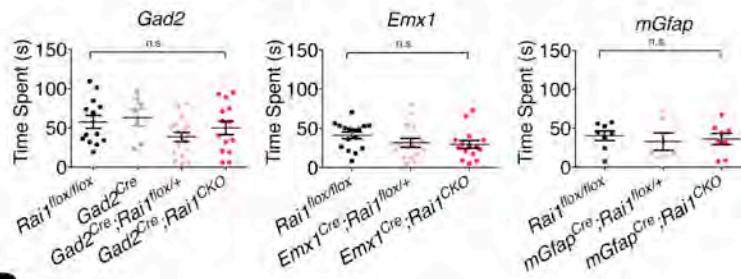
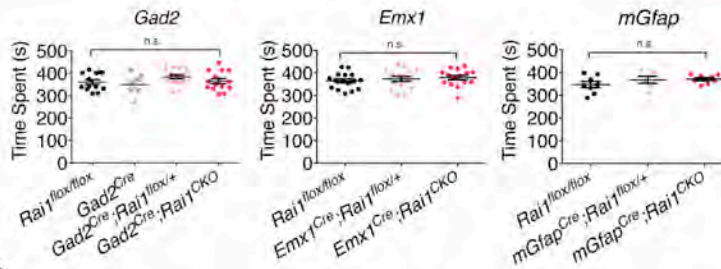
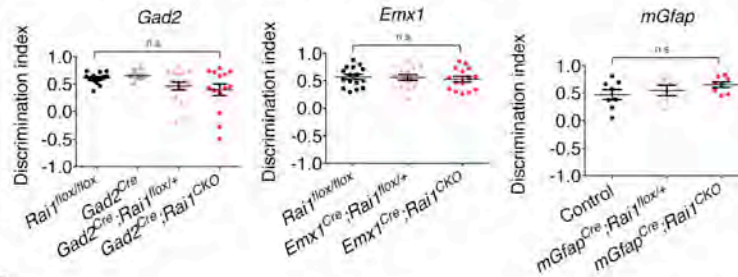
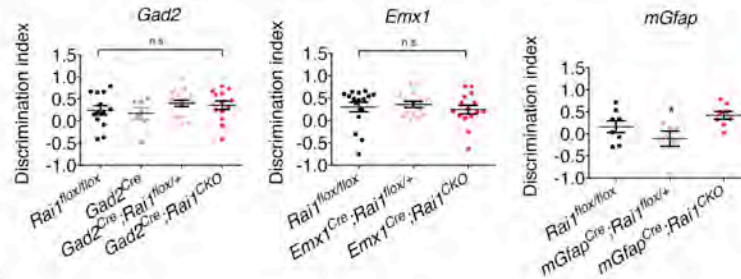
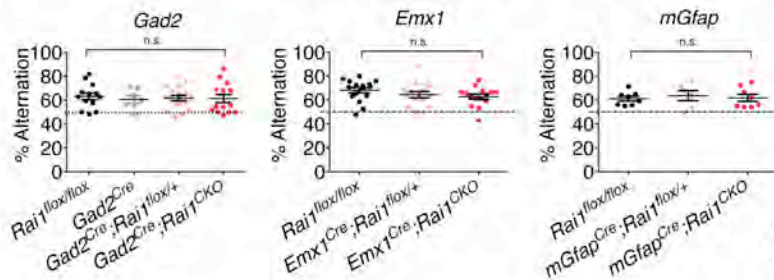
A**Elevated plus maze: Time spent in open arms****B****Elevated plus maze: Time spent in closed arms****C****Sociability: Mouse vs cup****D****Social discrimination: Novel vs familiar mice****E****Y-Maze: % Alternation**

Figure S6. Behavioral Characterization of *Rai1* Conditional Knockout, Related to Figure 5

(A–B) Time spent in the open (A) and closed (B) arms of an elevated plus maze do not differ between *Rai1^{flox/flox}*, *Gad2^{Cre};Rai1^{CKO}*, *Emx1^{Cre};Rai1^{CKO}*, and *mGfap^{Cre};Rai1^{CKO}* mice. Shown are mean ± SEM.

(C) The *Gad2^{Cre};Rai1^{CKO}*, *Emx1^{Cre};Rai1^{CKO}*, and *mGfap^{Cre};Rai1^{CKO}* mice have comparable sociability discrimination index as the *Rai1^{flox/flox}* mice. Shown are mean ± SEM.

(D) Social discrimination index is statistically indistinguishable between *Rai1^{flox/flox}*, *Gad2^{Cre};Rai1^{CKO}*, *Emx1^{Cre};Rai1^{CKO}*, and *mGfap^{Cre};Rai1^{CKO}* mice. The *mGfap^{Cre};Rai1^{flox/+}* group shows a decreased discrimination index due to an outlier mouse that spent most of its time with a familiar mouse. Shown are mean ± SEM.

(E) Alternation between arms of a Y-Maze is not different between *Rai1^{flox/flox}*, *Gad2^{Cre};Rai1^{CKO}*, *Emx1^{Cre};Rai1^{CKO}*, and *mGfap^{Cre};Rai1^{CKO}* mice. Shown are mean ± SEM.

Statistics: One-way ANOVA; n.s., not significantly different, * p < 0.05.

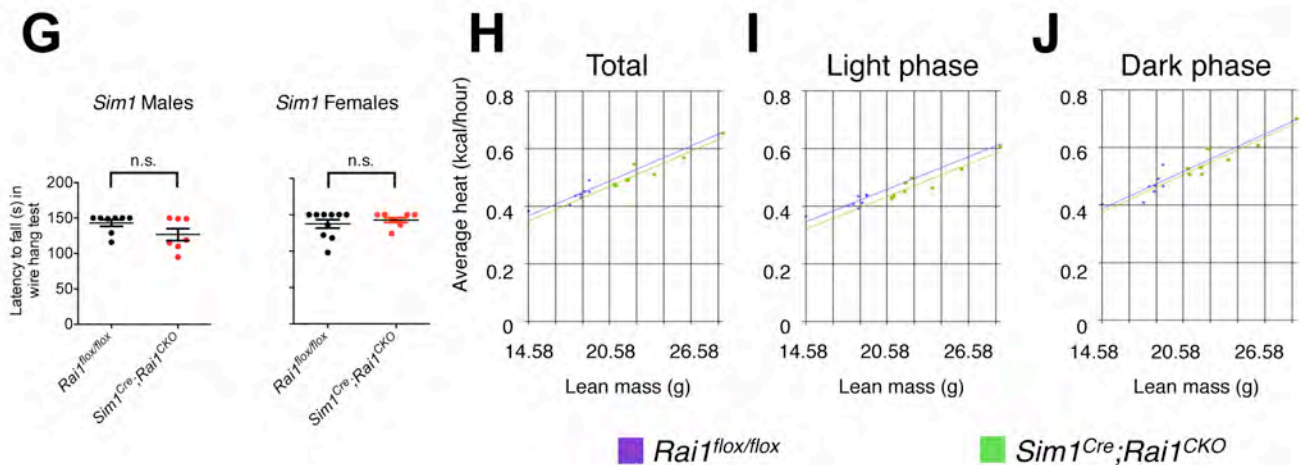
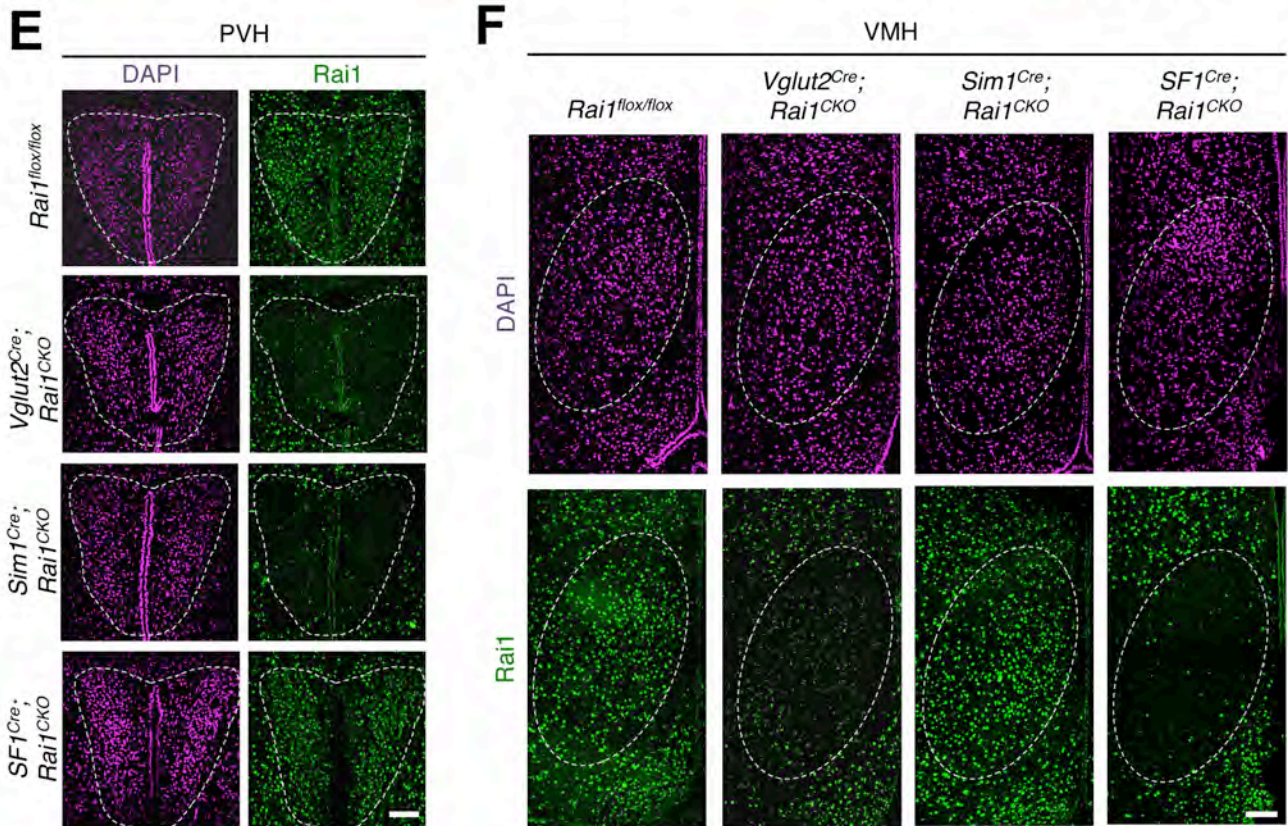
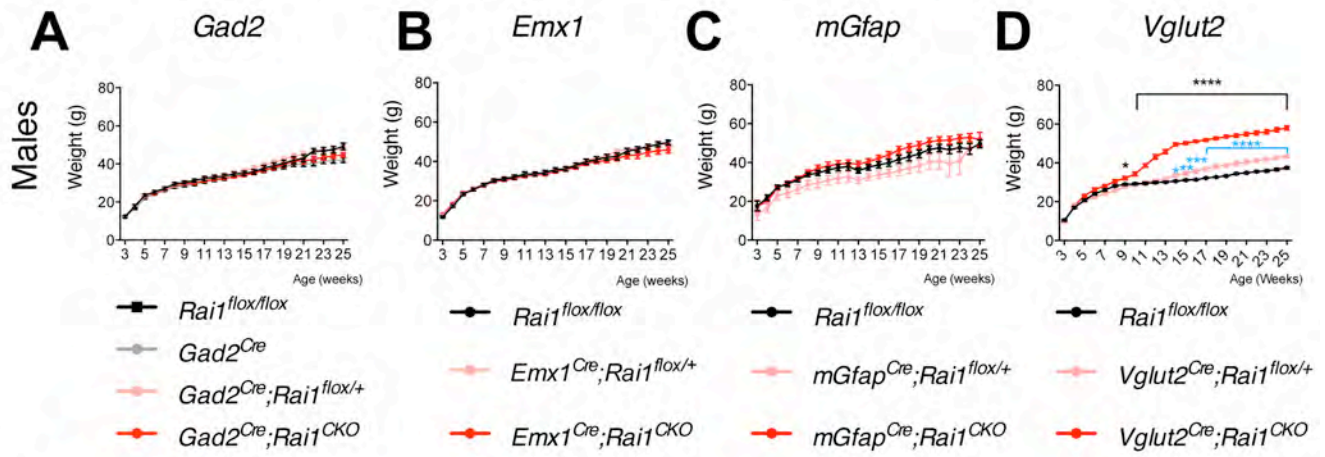


Figure S7. Characterization of Obesity *Rai1* Mutants, Related to Figures 6 and 7

(A-D) Mean (\pm SEM) body weights over time of male mice that lost one or both copies of *Rai1* in the *Gad2* (A, n=15-24 for each genotype), *Emx1* (B, n=15-16 for each genotype), *mGfap* (C, n=8-10 for each genotype), and *Vglut2* (D, n=8-11 for each genotype)-Cre lineages. Male *Vglut2^{Cre};Rai1^{flox/+}* and *Vglut2^{Cre};Rai1^{CKO}* mice become significant obese beginning at 14- and 9-weeks of age, respectively. Statistics: * p < 0.05, ** p < 0.01, *** p < 0.001, **** p < 0.0001, Tukey's post hoc test following significant two-way ANOVA.

(E) *Rai1* expression (green) in the hypothalamic PVH region (white dotted lines circled region), with DAPI staining (magenta, left). *Rai1* staining in the PVH is mostly lost in the *Vglut2^{Cre};Rai1^{CKO}* and *Sim1^{Cre};Rai1^{CKO}* mice, but not in the *Rai1^{flox/flox}* or *SF1^{Cre};Rai1^{CKO}* mice.

(F) *Rai1* expression (green) in the hypothalamic VMH region (white dotted circles), DAPI staining is shown in magenta. *Rai1* signal in the VMH is mostly lost in the *Vglut2^{Cre};Rai1^{CKO}* and *SF1^{Cre};Rai1^{CKO}* mice, but not the *Rai1^{flox/flox}* or *Sim1^{Cre};Rai1^{CKO}* mice.

(G) Motor function of *Sim1^{Cre};Rai1^{CKO}* mice analyzed by the wire hang test. Deletion of *Rai1* in *Sim1⁺* cells does not impair motor skills in either male or female mice. Shown are mean \pm SEM. p > 0.05, unpaired t-test.

(H-J) Multiple linear regression analysis (analysis of covariance, ANCOVA) was used to assess the impact of lean mass on energy expenditure. *Rai1^{flox/flox}* (purple dots) and *Sim1^{Cre};Rai1^{CKO}* (green dots) mice show similar energy expenditure during total (light + dark) (H, p = 0.2716), the light phase (I, p = 0.1248), and the dark phase (J, p = 0.6489) (n=8 for each genotype).

SUPPLEMENTAL TABLES (Excel files)

Table S1: Summary of Rai1-Tag co-localization with cell type-specific markers, related to Figure 1.

Table S2: Rai1 ChIP-seq sample information, related to Figure 2.

Table S3: Rai1 ChIP-seq quality control, related to Figure 2.

Table S4: Chromatin state discovery and characterization (ChromHMM) analysis, related to Figure 2.

Table S5: Differentially expressed genes of Rai1-deficient cortex and striatum identified by RNA-seq, related to Figure 3.

Table S6: Gene ontology analysis using down-regulated genes in Rai1-deficient cortex and striatum, related to Figure 3.

Table S7: Primers for ChIP-qPCR and quantitative RT-PCR, related to Figures 2 and 3, and Supplemental Experimental Procedures.

Table S8: RNA-seq sample information, related to Figure 3.

Table S9: Differentially expressed genes of Rai1-deficient hypothalamus identified by RNA-seq, related to Figure 7.

SUPPLEMENTAL EXPERIMENTAL PROCEDURES

Mouse Husbandry and Handling

All animal procedures followed animal care guidelines approved by Stanford University's Administrative Panel on Laboratory Animal Care (APLAC). For behavioral assays, the C57BL/6J:129X1/SvJ F1 hybrid mice were used. *Rai1*^{fllox/+} mice were backcrossed at least four generations onto C57BL/6J or 129X1/SvJ backgrounds; at least one backcross included mating of an inbred C57BL/6J or 129X1/SvJ male with an *Rai1*^{fllox/+} female to set the genetic background of the Y chromosome. *Nestin*^{Cre} (RRID:IMSR_JAX:003771), *Gad2*^{Cre} (RRID:IMSR_JAX:010802), *Vglut2*^{Cre} (RRID:IMSR_JAX:016963), *mGfap*^{Cre} (RRID:IMSR_JAX:012886), *Emx1*^{Cre} (RRID:IMSR_JAX:005628), and *SF1*^{Cre} (RRID:IMSR_JAX:012462) mice were obtained from the Jackson Laboratories. *Sim1*^{Cre} mice (RRID:IMSR_JAX:006395) were provided by Dr. B. Lowell (Beth Israel Deaconess Medical Center). All Cre mice were backcrossed at least four generations onto a C57BL/6J background.

Generation of the *Rai1-Tag* Mice

The targeting construct for producing the *Rai1-Tag* allele was generated by first cloning the 5' homology arm including the last three *Rai1* exons and a *loxP* site (with the stop codon of the last *Rai1* exon removed) into a pCR2.1-TOPO vector (Invitrogen) as backbone. Then, the following three partially overlapping PCR fragments were linked by In-Fusion cloning (Clontech): Fragment 1: a partial *loxP* site, 3X FLAG, and 5X myc tags which were designed to be in frame with *Rai1* ORF, followed by triple translational stop codons in tandem; Fragment 2: partial myc tag and triple stop codons, FRT-pSV40-Neo-pA, and a partial *loxP* site; Fragment 3: an intact *loxP* site and an EGFP sequence designed to be in frame with *Rai1* ORF after Cre-mediated recombination. The resulting fragment was subsequently cloned into an EcoRV site of the pCR2.1-TOPO vector containing the 5' homology arm previously described. The DTA cassette for negative selection was inserted with HindIII/KpnI sites, and the 3' homology arm was inserted with a NotI site. The final construct was linearized with PvuI restriction enzyme and electroporated into 129Sv/SvJ ES cells. The correctly targeted clones were identified by long-range PCR (LA Taq, TaKaRa) and DNA sequencing. Targeted ES cells were microinjected into BL/6 blastocysts, and chimeras with successful germ line transmission were identified by PCR and were used to expand the colony. The proper fusion of FLAG/myc tags and the Cre-dependent fusion of EGFP tag to the C terminal of *Rai1* cDNA was verified by extracting mRNA from the brain of *Rai1-Tag* mice with or without Cre expression, followed by cloning and sequencing (data not shown). ES cell manipulations and blastocyst injections were performed by the Stanford Transgenic Research Facility.

Generation of the *Rai1-flox* Mice

The targeting construct for production of the conditional *Rai1* allele was generated using conventional cloning approaches with a FRT5-pSV40-Neo-pA-FRT5 cassette and homology arms amplified by high-fidelity PCR (Phusion, Thermo Fisher Scientific) from 129X1/SvJ genomic DNA (Jackson Labs). Growth of the full targeting construct in bacteria at high copy number led to loss of the DNA segment between *loxP* sites, presumably due to the actions of endogenous bacterial recombinases. To circumvent this issue, the construct was sub-cloned into a bacterial artificial chromosome (BAC) vector prior to the final cloning steps, and the construct was maintained at 1-2 copy numbers per bacterial cell. After verification by sequencing, the construct was electroporated into 129Sv/SvJ ES cells. The correctly targeted clones were identified by long-range PCR (LA Taq, TaKaRa) and DNA sequencing. Targeted ES cells were microinjected into BL/6 blastocysts, and chimeras were mated to a germline-active Flp transgenic line to remove the neomycin resistance cassette. Pups lacking the Neo cassette were identified by PCR and were used to expand the colony. ES cell manipulations and blastocyst injections were performed by the Stanford Transgenic Research Facility.

Mouse Genotyping

The presence of an *Rai1*^{Tag} allele was detected using primers: forward 5'-ATATCATGGCCGACAAGCAGAAGA-3' and reverse 5'-TGGGCGCAGCTCTTCTTCCTC-3' that detects a 326-bp band. And the wild-type *Rai1* allele can be detected using primers: forward 5'-CTAGGGTGATTGCACAGTTCTTG-3' and reverse 5'-TGGGCGCAGCTCTTCTTCCTC-3' that detects a 138-bp band. For the *Rai1*-flox mice, the *Rai1*^{flox} and *Rai1*^Δ (null) alleles were identified using primers A-C: 5'-CAGAGTCCAGATGGCACTACAGGGG-3' (A, common forward), 5'-GTGAGCTCCCGCTGAAATGGACAGT-3' (B, wild-type and floxed reverse), and 5'-GGAGGTCTGCGCTTCAGGGCTTAAT-3' (C, Δ reverse). With these primers, *Rai1*⁺ produces a 396-bp band, *Rai1*^{flox} produces a 497-bp band, and *Rai1*^Δ produces a 261-bp band. The *Nestin*^{Cre}, *Gad2*^{Cre}, *Vglut2*^{Cre}, *mGfap*^{Cre}, and *Emx1*^{Cre} mice were genotyped with primers Cre-A 5'-CACCTGTTACGTATAGCCG-3' and Cre-B 5'-GAGTCATCCTTAGCGCCGTA-3' for a 300-bp Cre band, and primers IC 5'-CCAATCTGCTCACACAGGATAGAGAGGGCAGG-3' and IC- 5'-CCTTGAGGCTGTCCAAGTGATTCAGGCCATCG-3' for a 500-bp internal control band. The *SF1*^{Cre} mice were genotyped with primers oIMR6243 5'-CTGAGCTGCAGCGCAGGGACAT-3' and oIMR6244 5'-TGCGAACCTCATCACTCGTTGCAT-3' for a 250-bp Cre band, and primers oIMR8744 5'-CAAATGTTGCTTGTCTGGTG-3' and oIMR8745 5'-GTCAGTCGAGTGCACAGTTT-3' for a 200-bp internal control band. The *Sim1*^{Cre} mice were genotyped with primers Sim1-Cre-1 5'-CACGACCGGCAAACGGACAGAA-3', Sim1-Cre-2 5'-TGGGATTAGCGTGTTTCAACTGAGC-3', and Sim1-Cre-3 5'-TTTTGGTTTTGGATGAGTCTGTGGAG-3' for an internal control (600-bp) and a Cre (250-bp) band.

Protein Expression and Purification

GST-tagged protein was expressed in Rosetta (DE3) pLysS cells (Novagen). The cells were grown in LB medium at 37°C and then induced by 1 mM isopropyl β-D-1-thiogalactopyranoside (IPTG) at 25°C for overnight culture growth. The cells were lysed with lysis buffer (50 mM Tris pH 7.5, 150 mM NaCl, 0.05% NP-40), incubated on ice with 0.25 mg/ml lysozyme for 1 hour, and then sonicated with Branson Digital Sonifier (18% output for 10 seconds, 1 second sonication with 1 second break). Lysates were spun in 12,000 rpm at 4°C for 20 minutes, and then incubated with glutathione beads (Amersham) at 4°C for overnight. The beads were washed three times with lysis buffer, and the GST-tagged fusion protein was eluted with 10 mM Glutathione (Sigma). Finally, 20 mM Dithiothreitol (DTT) was added, and protein was aliquoted and stored in -80°C.

In Vitro Binding Assay

For nucleosome pull-down/Western assay, 1.5 μg of mononucleosomes purified from HeLa cells were incubated with 15 μg of GST-fused protein in binding buffer (300 mM NaCl, 0.1% NP-40, 50 mM Tris-HCl pH 7.5, 10% glycerol) at 4°C for overnight. 30 μl of washed glutathione beads were then added to the binding solution and incubated for one hour. Washed beads were denatured and subjected to 12% Bis-Tris gel electrophoresis and detected with an anti-H3 antibody (ab1791, Abcam, RRID:AB_1079). The purity and integrity of purified proteins were verified with SimplyBlue SafeStain (Thermo Fisher Scientific), the loading controls were blotted with an anti-GST-HRP antibody (GE Healthcare, RRID:AB_771429) using Western blot analysis.

Generation of Rai1 Antibody

Antibodies against the following Rai1 peptides were raised in rabbits by Thermo/Pierce custom antibody services: DKYHRGSKSLQGRPAFPSY (Rai1-76:94), RPDGPADPAKQGPLRTSAR (Rai1-1738:1756). Antisera from six rabbits injected with either Rai1-76:94 or Rai1-1738:1756 were tested by immunohistochemistry, and antisera from two rabbits that produced the highest signal-to-background ratios were affinity purified using the immunizing peptides. The two resulting affinity purified antibodies, ab15 (against Rai1-76:94) and ab20 (against Rai1-1738:1756), were further tested by immunohistochemistry.

In Situ Hybridization Followed by Immunostaining

ISH probes were generated as previously described (Weissbourd et al., 2014). 50 μ m coronal sections containing the cortex were collected into a 24-well plate containing PBS. The sections were fixed for 15 minutes in 4% paraformaldehyde in PBS at room temperature, rinsed with PBS, and incubated for 15 minutes with 3% hydrogen peroxide (Sigma, 216763) in PBS. Sections were rinsed with PBS and incubated with 7 μ g/ml Proteinase K (Life Technologies, 25530-049) in 10 mM Tris-HCl, pH 7.4, 1 mM EDTA for 10 minutes at 37°C. After fixing again with 4% paraformaldehyde in PBS for 10 minutes and rinsing with PBS, the sections were incubated with 0.25% acetic anhydride in 0.1 M triethanolamine, pH 8.0, for 15 minutes at room temperature and washed with PBS. Probes were diluted (~1:1000) with the hybridization buffer (50% formamide, 10 mM Tris-HCl pH 8.0, 200 μ g/ml tRNA, 10% Dextran Sulfate, 1x Denhalt's solution, 600 mM NaCl, 0.25% SDS), mixed well, preheated at 85°C for 5 minutes, and applied to sections (300–500 μ l/well). After 16-20 hours of incubation at 60°C, the sections were washed, first with 2x SSC-50% formamide, then with 2x SSC, and finally with 0.2x SSC twice for 20 minutes at 65°C. Sections were equilibrated in Tris Buffer (100 mM Tris-HCl, pH 7.5, 150 mM NaCl) for 5 minutes at room temperature, then blocked in Tris Buffer + 0.5% Blocking Reagent (Perkin Elmer, cat# 11096176001) for 30 minutes at room temperature. Then, sections were incubated with anti-DIG-POD Fab fragments (Roche, cat# 11633716001, AB_514499, lyophilized and diluted in 1 ml of water) at 1:2000 in Tris Buffer + 0.5% Blocking Reagent for 30 minutes at room temperature. Sections were washed with Tris Buffer + 0.05% Tween20 (Sigma, P9416). Next, a TSA Plus Cyanine 3 Kit (Perkin Elmer, NEL744001KT) was used to detect in situ signal. Briefly, Cy3-Tyramide was diluted 1:50 in amplification reagent and applied to the sections for 5–10 minutes at room temperature. Sections were then washed in Tris Buffer + 0.05% Tween20, and incubated with Tris Buffer + 0.05% Tween20 + anti-myc antibody (1:1000, Novus Biologicals, NB600-338, RRID:AB_10001879, for 3 days at 4°C). Sections were washed with Tris Buffer + 0.05% Tween20, then incubated with FITC conjugated donkey anti-goat antibodies (1:500; Jackson ImmunoResearch, RRID:AB_2340400) for an additional 1–2 hours, and washed with PBS three times for 10 minutes. Finally the sections were treated with PBS containing 4',6-diamidino-2-phenylindole dihydrochloride (DAPI; Sigma-Aldrich, D8417) for 20 minutes and mounted with cover glass using Fluorogel (Electron Microscopy Sciences, Cat#17985-10).

PCR Primers used to Prepare Templates for ISH Probes: T3 polymerase recognition site is indicated by underline.

Vglut1

5'-CTGGCAGTGACGAAAGTGAA;

5'- AATTAACCCTCACTAAAGGGGACACAACAAATGGCCACTGA

Gad1

5'-CACAAACTCAGCGGCATAGA;

5'- AATTAACCCTCACTAAAGGGGGGACGAGCAACATGCTATGG

Gad2

5'-GGGATGTCAACTACGCGTTT;

5'- AATTAACCCTCACTAAAGGGTGCATCAGTCCCTCCTCTCT

Immunostaining and Antibodies

For immunostainings that involve anti-Rai1 antibody, mice were euthanized with isoflurane, and their brains were rapidly dissected, immersed in Optimal Cutting Temperature (OCT) compound (Tissue-Tek, Sakura), and frozen by immersion in a dry ice/ethanol bath. 8 μ m thick sections were mounted to Superfrost plus slides, and washed three times in phosphate buffered saline (PBS), incubated 10 minutes at –20°C in pre-cooled acetone, washed four times in PBS, and then blocked for 2 hours at room temperature in 10% normal donkey serum (NDS) in PBS. Slides were further incubated overnight at 4°C with primary antibodies in 10% NDS in PBS, washed 4 times for 5 minutes in PBS, incubated for 2–3 hours at room temperature with secondary antibodies in 10% NDS in PBS, washed 4 times for 5 minutes in PBS, incubated for ~10 minutes in ~1:30000 dilution of 5 mg/mL DAPI in PBS, washed

once for 5 minutes in PBS, and coverslipped in Fluoromount-G (SouthernBiotech). Immunostainings that do not involve anti-Rai1 antibody followed previously described protocols (Guenther et al., 2013). The following antibodies were used: mouse anti-FLAG M2 (1:1000, Sigma, RRID:AB_439685), mouse anti-HDAC2 antibody (1:1500, Abcam, RRID:AB_2118547), mouse anti-S100 β (1:1000, Sigma, RRID:AB_477499), mouse anti-NeuN (1:1000, EMD Millipore, RRID:AB_177621), rabbit anti-Ki67 (1:1000, Abcam, AB_302459), rabbit anti-H3 (1:2000, Abcam, RRID:AB_302613), rabbit anti-Rai1 (1:250, custom made), goat anti-myc (1:1000, Novus Biologicals, RRID:AB_10001879), chicken anti-GFP (1:2500, Aves Labs, RRID:AB_10000240). Secondary antibodies conjugated to 488 (Donkey anti-chicken, RRID:AB_2340375; Donkey anti-rabbit, RRID:AB_2313584; Donkey-anti-mouse, RRID:AB_2340846; Donkey-anti-goat, RRID:AB_2340428) or Cy3 (Donkey anti-rabbit, RRID:AB_2307437; Donkey-anti-mouse, RRID:AB_2315777; Donkey-anti-goat, RRID:AB_2340411)(Jackson Immunoresearch) were diluted 1:500~1:2000 from 50% glycerol stocks.

Chromatin Immunoprecipitation-sequencing (ChIP-seq) and ChIP-qPCR

8-week-old cortices of male *Rai1*^{Tag/+} mice were used for ChIP-seq experiment. Cortical tissues were cross-linked with 1% formaldehyde for 10 minutes at room temperature, followed by quenching with 0.125 M glycine and washed twice with cold PBS containing 0.5 mM PMSF. Chromatin was sonicated to an average size of 0.3–1 kb using Bioruptor (Diagenode). A total of 10 μ g of anti-FLAG M2 antibody (Sigma, RRID:AB_439685) was added to the sonicated chromatin and incubated overnight at 4°C. Subsequently, 50 μ l of protein G Dynal magnetic beads were added to the ChIP reactions and incubated for 6 hours at 4°C. Magnetic beads were washed and chromatin eluted, followed by reversal of crosslinks and DNA purification (ChIP DNA clean & Concentrator kit, ZYMO research). ChIP-qPCR was performed with independently isolated samples to confirm ChIP-seq results. Chromatin was pulled-down with IgG (negative control) or anti-FLAG antibody, and then amplified with sequence specific primers. Quantitative PCR reactions were conducted using SsoFast EvaGreen Supermix (Bio-Rad) on a StepOnePlus Real-Time PCR System (Thermo-Fisher Scientific).

Data Analysis for ChIP-seq

The libraries were sequenced using HiSeq 2500 sequencing system (Illumina), yielding 32-39 million of 2 X 50 base paired-end reads for both ChIP and control (input) libraries. The paired-end reads were mapped to the mouse reference genome (mm9) using bowtie2 (version 2.2.3) (Langmead and Salzberg, 2012) with “—very-sensitive” and default parameters. Read pairs, which aligned concordantly to the genome and had a mapping quality more than 10, were kept for following analyses. Read pairs mapped to mitochondrial DNA were discarded. Redundancy read pairs from PCR duplication were also removed afterward using Picard tools (version 1.134, <http://broadinstitute.github.io/picard>). Peak regions were identified by MACS2 (Version 2.1.0) with the parameters “-g mm -p 0.001 --fix-bimodal” for each ChIP and Input replicate pair. Consistency analysis of the peaks identified from replicas was done by IDR package following the guideline (Li et al., 2011). Consistency peaks with IDR score lower than 0.05 were selected as high-confidence peaks and kept for the following genome-wide analyses. The final bam file from replicas were merged and then converted into normalized BigWig files using bedtools (v2.17.0) (Quinlan and Hall, 2010) for visualization in the UCSC genome browser. The high-confidence peaks were annotated to different genome features and enrichment score were calculated for each feature using Homer (Heinz et al., 2010). Alignment file of histone modification data were downloaded from ENCODE ftp sites (<ftp://hgdownload.cse.ucsc.edu/goldenPath/mm9/encodeDCC/wgEncodeLicrHistone>). Six histone modification markers as well as Pol2 and CTCF ChIP-seq data were collected. H3K27ac, H3K4me1, H3K4me3, Pol2 and CTCF were derived from 8-week-old cortex and H3K27me3, H3K36me3 and H3K9me3 were derived from the whole brain at E14.5.

The alignment files (in bam format) were first converted into bed file and then analyzed for chromatin state discovery and characterization following the guideline of ChromHMM (Ernst and Kellis, 2012). To identify the potential binding consensus sequence of Rai1, the top 20% of high-confidence peaks were

used to perform a de novo motif search using Homer with the parameters “-size given -mask”. Normalized read intensity of Rai1 ChIP-seq and other ChIP-seq data around gene body or Rai1 binding regions were plotted by ngsplot (Shen et al., 2014). The same data sets of H3K4me3 and Pol2 from ENCODE were used. The ChIP-seq data of Zfx and GFP were downloaded from GEO database (accession numbers GSM288352 and GSM288358). The raw data were mapped with bowtie2 and convert into bam files using samtools (Version 0.1.19).

RNA-seq and qRT-PCR

Cortex of male *Nestin^{Cre};Rai1^{CKO}* mice, striatum of male *Gad2^{Cre};Rai1^{CKO}* mice, and hypothalamus of male *Vglut2^{Cre};Rai1^{CKO}* mice, as well as their *Rai1^{fllox/fllox}* littermates (control) were used for RNA-seq experiments. Total RNA was extracted by TRizol reagent (Life Technologies) and phenol-chloroform-isoamyl alcohol (Life Technologies). The residual DNA was removed with on-column DNase digestion (Qiagen) for 30 minutes and RNA was further purified using RNeasy Kit (Qiagen). Total RNA from 2 biological replicas of each genotype was used. Ribosomal RNA was depleted with Ribo-Zero rRNA removal kits (Illumina). The barcoded libraries were prepared with illumine RNA preparation kit according to manufacturer’s instruction. Quantitative RT-PCR (qRT-PCR) was performed with independently isolated samples to confirm RNA-seq results. After isolation of total RNA, mRNA was reverse-transcribed with SuperScript III First-Strand Synthesis System (Thermo-Fisher Scientific). Quantitative PCR reactions were conducted using SsoFast EvaGreen Supermix (Bio-Rad) on a StepOnePlus Real-Time PCR System (Thermo Fisher Scientific).

Data Analysis for RNA-seq

The libraries were sequenced using HiSeq 2500 sequencing system (Illumina), yielding 30–60 million of 2 X 100-bp paired-end reads per sample. The adaptor sequences were first scanned and removed for the raw reads by cutadapt (version 1.6) (Martin, 2011). The trimmed sequences were mapped to mouse reference genome (mm9) using Tophat2 with parameters “-l 1000000 --max-coverage-intron 1000000 --max-segment-intron 1000000 --no-coverage-search --b2-very-sensitive --microexon-search”. Read pairs, which were aligned concordantly to the genome, were counted according to the RefGene annotation from UCSC using DEGseq (v0.50.1). The longest isoform were selected when there are multiple isoforms. Differentially expressed genes between conditional knockout and control for each cell type were analyzed by DESeq2 (Love et al., 2014). Genes with FDR < 0.1 were selected as differential expression genes for following analysis. Gene ontologies enrichment was tested by merging down-regulated gene in either cortex or striatum using DAVID (Huang da et al., 2009). For list of differentially expressed genes identified in *Rai1*-deficient cortex and striatum, see Table S5. For details of RNA-seq samples, see Table S8. For list of differentially expressed genes identified in *Rai1*-deficient hypothalamus, see Table S9. Due to potential incomplete deletion of *Rai1* exon 3 in *Gad2^{Cre};Rai1^{CKO}* striatum and *Vglut2^{Cre};Rai1^{CKO}* hypothalamus, and the up-regulation of *Rai1* exons 4–6 in conditional mutants, *Rai1* was identified as an up-regulated gene in these conditional mutants. Our qRT-PCR experiments (Figures 3B, 7D, and S3E) have confirmed that *Rai1* exon3 was indeed down-regulated in these samples. Western blot also confirmed loss of Rai1 protein in conditional mutants (Figure S3C). RNA splicing algorithm (data not shown) independently confirmed the deletion of *Rai1* exon 3 in *Gad2^{Cre};Rai1^{CKO}* striatum and *Vglut2^{Cre};Rai1^{CKO}* hypothalamus. Therefore, we removed *Rai1* from the DEG list to prevent confusion.

Mouse Behavioral Assays

Activity Chamber

Mice were placed for 10 minutes in the center of a 43.2 x 43.2 cm square arena in a 66 x 55.9 x 55.9 cm sound-attenuating chamber under dim red light. Mice were allowed to move freely in the chamber, and the time spent in the center versus periphery of the arena, distance moved, average velocity, and vertical movement were determined from infrared sensors using an automated system. At the end of each trial, the surface of the arena was cleaned with 1% Virkon.

Y maze

Mice were placed in a Y-shaped maze consisting of white plastic arms positioned 120° apart radially. All arms were 12.7 cm high and 7.62 cm wide; two arms were 15.24 cm in length, and one arm was 20.32 cm in length. Each mouse was allowed to explore the maze for 5 minutes, and the order of arm entries was recorded. The sequence of arm entries was broken into overlapping, consecutive triads (total number of triads = total number of arm entries – 2). The percent alternation was defined as: (number of triads containing entry into all three arms / total number of triads) X 100.

Elevated Plus Maze

Mice were placed in the center of an elevated + shaped maze with two open arms (i.e., without walls) and two closed arms (i.e., with walls). Mice were allowed to explore for 5 minutes, and their positions were monitored using an automated tracking system (EthoVision, Noldus). The time spent in open versus closed arms and the number of entries into each arm, along with other parameters, were calculated. The surfaces and walls of the maze are cleaned with 1% Virkon to eliminate odor.

Cat Walk

Mice were trained to traverse a linear track (CatWalk, Noldus) by placing their homecage at the opposite end of the track. Multiple trials were performed until each mouse had completed three trials in which they traversed the track continuously without stopping. The positioning of the paws during each step was automatically determined using a video-based system, and a variety of gait parameters, including distances between paws, step patterns, and limb swing speeds were determined.

Vertical Pole Descent Test

Mice were placed at the top of a coarse, vertical wooden pole (diameter: 1 cm; height: 55 cm), and the time required to descent was recorded. After a practice trial, 4 test trials were conducted with an inter-trial interval of ~2 minutes. If the mouse did not descend or dropped or slipped down the pole without climbing, a descent time of 60 seconds was recorded.

Wire Hang

Mice were placed on a wire grid, which was inverted such that the mice were hanging upside down by all four paws approximately 50 cm above a cage with bedding. The latency to fall was recorded, and each trial was terminated after 150 seconds. Mice were given three trials per day.

Sociability and Social Discrimination

Mice were placed in a testing cage containing two empty inverted cups and were allowed to habituate for 20 minutes. An unfamiliar mouse (C57BL/6 juvenile) was then placed under one of the cups, and the time spent by the subject mouse investigating the two cups was quantified (sociability). Sociability was calculated by discrimination Index= $(M - C) / (M + C)$. M= time spent sniffing a mouse, C= time spent sniffing a cup. A second unfamiliar juvenile was then placed under the cup in the position of the 1st mouse when introduced to the cage and the familiar mouse was moved to where the empty cup had previously been located (social discrimination). In this task the time spent sniffing novel and familiar mice was quantified. Social discrimination was calculated by discrimination Index= $(N - F) / (N + F)$. N= time spent sniffing novel mouse, F= time spent sniffing familiar mouse. Discrimination index was then compared across genotypes using one-way ANOVA.

Fear Conditioning

On Day 1 (training), mice were placed in Context A and after 3 minutes, they were presented with a tone (75 dB, 2 kHz, 20 sec) followed 18 seconds later by a footshock (0.5 mA, 2 seconds); mice received a total of five tone-shock pairings with an inter-tone interval (from the end of one tone to the start of the next tone) of 80 seconds. On Day 2 (cued recall) mice were placed for 3 minutes in Context B, which had different olfactory, somatosensory, and visual cues from Context A. They were

subsequently presented with three tone presentations (80 seconds inter-tone interval) without any shocks. On Day 3 (contextual recall), mice were placed in Context A for 5 minutes without any tone presentation. Freezing, defined as complete lack of motion for at least 0.75 seconds, was quantified on all three days by an automated video scoring system (FreezeFrame, Actimetrics).

Hot Plate Assay

Mice were placed on a hot plate (Model 39, IITC) heated to either 50°C or 55°C, and the latency to exhibit pain behavior (paw lifting, paw licking, or jumping) was recorded. Mice were tested in three trials per temperature.

Energy Homeostasis Analyses

Home Cage Food Intake

Manual food intake measurements were made every 2–3 days for 1 week. Food was weighed prior to placement in the cage. After 2–3 days, food remaining in the hopper and any significant spillage inside the cage were combined and weighed. The difference is the amount of food intake during the specific timeframe.

Adiposity

Body composition (lean and fat mass) was measured by Dual Energy X-ray absorptiometry (DEXA) (Lunar PIXImus Densitometer, GE Medical Systems). Brown and white adipose tissues from different depots (gonadal, subcutaneous, retroperitoneal, and mesenteric) were dissected and weighed. Tissue weights were recorded.

Indirect Calorimetry

Energy expenditure and physical activity were evaluated in age matched (30-32 weeks) female *Rai1^{flox/flox}* and *Sim1^{Cre};Rai1^{CKO}* mice by indirect calorimetry in the CLAMS (Comprehensive Lab Animal Monitoring System, Columbus Instruments). Animals were acclimated to the facility for at least 1 week, and then acclimated to the CLAMS cages and powdered diet (2018 Teklad Global 18% Protein Rodent Diet) for 48 hours and to the light and temperature-controlled chamber for 24 hours prior to testing. Analyzed data constitutes data collected from 48 hours of continuous measurement (2 light/2 dark cycles). Oxygen consumption and carbon dioxide production were measured and used to calculate energy expenditure (or heat production, kilocalories (kcal)) and respiratory exchange ratio (RER: VCO_2 / VO_2). Cage-mounted sensors detect and record measurements of physical activity (beam breaks). Multiple linear regression analysis (analysis of covariance, ANCOVA) was used to assess the impact of covariate (lean mass) on energy expenditure.

Reagents and Data Sharing

The following mouse lines will be available from The Jackson Laboratory: *Rai1-Tag* (JAX#029101) and *Rai1-flox* (JAX#029103). Plasmids are deposited to Addgene. Sequence data are deposited at NCBI GEO GSE81207.

SUPPLEMENTAL REFERENCES

Guenthner, C.J., Miyamichi, K., Yang, H.H., Heller, H.C., and Luo, L. (2013). Permanent genetic access to transiently active neurons via TRAP: targeted recombination in active populations. *Neuron* 78, 773-784.

Huang da, W., Sherman, B.T., and Lempicki, R.A. (2009). Systematic and integrative analysis of large gene lists using DAVID bioinformatics resources. *Nat Protoc* 4, 44-57.

Langmead, B., and Salzberg, S.L. (2012). Fast gapped-read alignment with Bowtie 2. *Nat Methods* 9, 357-359.

Li, Q.H., Brown, J.B., Huang, H.Y., and Bickel, P.J. (2011). Measuring Reproducibility of High-Throughput Experiments. *Annals of Applied Statistics* 5, 1752-1779.

Love, M.I., Huber, W., and Anders, S. (2014). Moderated estimation of fold change and dispersion for RNA-seq data with DESeq2. *Genome Biol* 15, 550.

Martin, M. (2011). Cutadapt removes adapter sequences from high-throughput sequencing reads. 2011 17.

Quinlan, A.R., and Hall, I.M. (2010). BEDTools: a flexible suite of utilities for comparing genomic features. *Bioinformatics* 26, 841-842.

Shen, L., Shao, N., Liu, X., and Nestler, E. (2014). ngs.plot: Quick mining and visualization of next-generation sequencing data by integrating genomic databases. *BMC Genomics* 15, 284.

Weissbourd, B., Ren, J., DeLoach, K.E., Guenthner, C.J., Miyamichi, K., and Luo, L. (2014). Presynaptic partners of dorsal raphe serotonergic and GABAergic neurons. *Neuron* 83, 645-662.